

Fully GPU-Accelerated, Matrix-Free Immersed Boundary Method for Fluid-Structure Interaction in Complex Hyperelastic Cardiac Models

Pengfei Ma¹⁻³, Li Cai^{1-3*}, Xuan Wang¹⁻³, and Hao Gao⁴

¹Xi'an Key Laboratory of Scientific Computation and Applied Statistics, China

²NPU-UoG International Cooperative Lab for Computation and Application in Cardiology, China

³School of Mathematics and Statistics, Northwestern Polytechnical University, China

⁴School of Mathematics and Statistics, University of Glasgow, UK

*Corresponding author, caili@npu.edu.cn

Abstract

In the field of cardiac fluid-structure interaction (FSI), the immersed boundary (IB) method has become the leading approach, effectively handling large deformations while avoiding the need for mesh regeneration. The latest trend of developing faster algorithms for the IB method on the latest heterogeneous parallel computing platform is one of the most promising directions for achieving personalized cardiovascular diagnosis and treatment. **However, the heart's soft tissue, modeled as a nonlinear fiber-reinforced hyperelastic material, requires additional projection steps to ensure the stability of the IB method.** These steps involve sparse matrix storage and computation, significantly degrading GPU performance. In this paper, we proposed an algorithm of the nodal immersed boundary method on the GPU, ensuring IB stability while eliminating finite element space projections. Furthermore, our algorithm fully avoids sparse matrix storage and computation in the Navier-Stokes equation solver. We also proposed several GPU-specific optimizations, such as leveraging constant memory for storing nodal basis function values and derivatives at Gauss quadrature points, as well as utilizing texture memory for the convective term in the Navier-Stokes equations. Our algorithm achieves maximum GPU utilization while preserving the mechanical complexity of soft tissue and maintaining IB method stability. Benchmark tests show that compared to a parallelized 20-core CPU implementation, our GPU-accelerated solution delivers comparable accuracy while achieving a $100\times$ speedup on a single GPU. Crucially, this advancement reduces simulation times for mitral and tricuspid valve models from days to mere hours, paving the way for clinical adoption.

Keywords: immersed boundary method, fluid structure interaction, GPU-Acceleration, computational cardiology, fiber-reinforced hyperelasticity

1 Introduction

Fluid-structure interaction (FSI) modeling plays a pivotal role in cardiovascular biomechanics as it enables the investigation of interactions between cardiovascular structures and blood flow. This capability provides critical theoretical support for understanding disease progression mechanisms and evaluating potential therapeutic interventions.^{1–7} Among the various numerical approaches for solving FSI problems, the immersed boundary (IB) method has emerged as a highly effective computational framework in cardiovascular research since its pioneering development.^{8,9} The IB method adopts a hybrid Eulerian–Lagrangian formulation, endowing it with two significant advantages for cardiovascular modeling. First, it inherently accommodates large deformations of biological tissues, thereby avoiding the mesh distortion issues frequently encountered in traditional conforming mesh methods. Second, it facilitates accurate stress computation for complex anatomical geometries represented in the Lagrangian framework. These computational strengths, combined with decades of continuous methodological refinements,^{10–12} have elevated the IB method from a specialized technique to a mainstream approach for solving FSI problems in biological systems. Modern IB implementations exhibit remarkable versatility, supporting a wide range of applications—from valvular dynamics to ventricular contraction—while maintaining numerical accuracy and stability under physiologically realistic flow conditions.

Early implementations primarily relied on multi-CPU architectures, with notable distributed-memory frameworks—such as the IBAMR (Immersed Boundary Adaptive Mesh Refinement) platform—demonstrating strong scalability on high-performance computing clusters.¹³ These CPU-based approaches tackled fundamental challenges related to load balancing and inter-processor communication in FSI systems.¹⁴ With the rapid evolution of general-purpose graphics processing unit (GPU) computing, GPUs have emerged as a powerful platform for accelerating large-scale parallel simulations.¹⁵ Nonetheless, widespread adoption of GPU-based IB solvers began relatively late (around 2011¹⁶), largely due to the inherent complexity of coupling fluid dynamics, solid mechanics, and their interactions. Significant progress has been made only in recent years, with several studies showcasing efficient GPU-accelerated IB implementations for cardiac FSI applications.^{17–19}

Current GPU-accelerated implementations of the IB method primarily support structures with prescribed kinematics¹⁸ or rely on simplified constitutive models, such as fiber-only or membrane-based formulations.¹⁷ To date, IBAMR remains the most comprehensively validated IB framework for cardiovascular FSI, particularly through its immersed boundary–finite element (IBFE) module.¹³ The IBFE module is an implementation of the formulations developed by Boffi et al.¹⁰ It incorporates hyperelastic constitutive models within a continuum mechanics framework, grounded in the principle of virtual work, derived from finite-deformation continuum mechanics. A key advantage of this formulation is its compatibility with a wide range of constitutive models, which can be parameterized directly from experimental data. This flexibility enables close agreement between numerical simulations and physical experiments, as shown in the work of Lee et al.²⁰ In this work, we also adopt the continuum-based IB formulation introduced by Boffi et al.¹⁰ Unlike membrane or fiber-network models, soft cardiac tissue is more accurately represented as a fiber-reinforced hyperelastic composite with finite volume, in which collagen forms a structural scaffold embedded with aligned myocardial fibers. This detailed representation captures the anisotropic and nonlinear mechanical behavior essential for realistic cardiac simulations. However, the increased fidelity of this modeling approach introduces substantial numerical challenges. In particular, energy conservation within the IBFE framework requires a projection step to preserve the duality between velocity interpolation and force spreading.¹¹ Moreover, projecting forces into the finite element space involves solving sparse linear systems resulting from the finite element discretization. These operations inherently constrain the parallel scalability of cardiac IB simulations, especially at physiologically realistic resolutions. Consequently, achieving ideal speedup on GPU architectures becomes highly challenging. To our knowledge, this work presents the first fully GPU-accelerated implementation of the IB model proposed by Boffi et al.¹⁰

In this paper, we propose a fully GPU-accelerated IB method for FSI in complex cardiac models. This method builds on the recently proposed nodal immersed finite element-finite difference method,²¹ which eliminates the need for projection steps in the finite element space and thus overcomes major barriers to parallel efficiency. The key idea involves using nodal coupling to implement interpolation and spreading operators, thereby eliminating global dependencies among unknowns in Lagrangian configuration, while preserving the duality of the operators. This

approach enables the development of a fine-grained, GPU-optimized algorithm that aligns with hardware characteristics throughout the entire simulation pipeline. The method achieves stable and accurate FSI simulations in fiber-reinforced hyperelastic materials. To support this, we decompose the Navier–Stokes equations into a Poisson equation and a Helmholtz equation.²² The former is solved using geometric multigrid methods, and the latter via in-place red–black Gauss–Seidel iterations. Semi-Lagrangian discretization of convection terms is efficiently implemented using GPU texture memory. Furthermore, we introduce a memory-efficient structural solver that stores second-order finite element basis functions and their derivatives at Gauss quadrature points in the GPU’s constant memory. This design enables rapid per-element force computations with minimal global memory access, ensuring scalability and performance. The main contributions of this study can be summarized as follows:

- Propose a novel, fully GPU-accelerated IB method for FSI in cardiac models featuring anatomically realistic, fiber-reinforced hyperelastic materials.
- We redesign the algorithm with a fine-grained, GPU-optimized architecture that leverages constant memory, global memory, and texture memory for high computational efficiency.
- We perform a rigorous performance evaluation, demonstrating 50×–100× speedup compared to a 20-core parallel IBAMR implementation. Our method enables clinically viable cardiac FSI simulations on a single GPU in just a few hours—capabilities previously infeasible using traditional CPU-based frameworks.

The subsequent sections of this paper are organized as follows: Section 2 presents the mathematical theoretical foundation of the IB method. Section 3 systematically describes the numerical discretization process of the IB method and explores its efficient implementation on GPUs. Section 4 employs the Cook’s membrane benchmark to systematically validate the computational accuracy and efficiency of the proposed method. Section 5 applies this method to cardiac mechanics, including the dynamic simulation of the left ventricle (LV), aortic valve (AV), and mitral valve (MV), and verifies its computational advantages in complex FSI problems through comparison with existing results. Finally, Section 6 summarizes the main findings of this study and discusses future research directions.

2 Immersed Boundary Formulation

2.1 Continuous equations of motion

In the framework of the IB method, the continuous formulation of the FSI system describes the coupled dynamics between the fluid and the immersed structure within a fixed domain. Let Ω be the computational domain, and B_t be the region occupied by the structure at time t . The computational domain uses fixed Eulerian coordinates $\mathbf{x} = (x_1, x_2, x_3) \in \Omega$, while the reference configuration of the structure employs Lagrangian reference coordinates $\mathbf{X} = (X_1, X_2, X_3) \in B_r$, where B_r is the region occupied by the structure at time $t = 0$. The transformation from the reference region B_r to the current region B_t is described by a bijection $\mathcal{X}(\mathbf{X}, t) : B_r \mapsto B_t$, which characterizes the deformation of the structure, such that

$$\mathbf{x} = \mathcal{X}(\mathbf{X}, t) \quad \text{for all } \mathbf{X} \in B_r.$$

Thus, the deformation gradient tensor is defined as:

$$\mathbb{F}(\mathbf{X}, t) = \frac{\partial \mathcal{X}}{\partial \mathbf{X}}(\mathbf{X}, t),$$

and $J(\mathbf{X}, t) = \det(\mathbb{F}(\mathbf{X}, t))$ is the determinant of $\mathbb{F}(\mathbf{X}, t)$.

Within the Eulerian formulation, the Cauchy stress tensor $\boldsymbol{\sigma}(\mathbf{x}, t)$ of flexible structures in an FSI system is expressed as:

$$\boldsymbol{\sigma}(\mathbf{x}, t) = \boldsymbol{\sigma}^f(\mathbf{x}, t) + \begin{cases} \boldsymbol{\sigma}^e(\mathbf{x}, t), & \mathbf{x} \in B_t, \\ 0, & \mathbf{x} \in \Omega/B_t, \end{cases}$$

where $\boldsymbol{\sigma}^e(\mathbf{x}, t)$ is the elastic component of the stress tensor that exists only in the solid domain, and $\boldsymbol{\sigma}^f(\mathbf{x}, t)$ is the fluid-like component of the stress tensor that exists everywhere in Ω . To describe the elastic properties of the structure in the Lagrangian coordinate system, $\boldsymbol{\sigma}^e(\mathbf{x}, t)$ is written as

$$\boldsymbol{\sigma}^e(\mathbf{x}, t) = \boldsymbol{\sigma}^e(\mathcal{X}(\mathbf{X}, t), t) = J^{-1}(\mathbf{X}, t)\mathbb{P}(\mathbf{X}, t)\mathbb{F}^T(\mathbf{X}, t),$$

where $\mathbb{P}(\mathbf{X}, t)$ represents the first Piola-Kirchhoff stress tensor. For the hyperelastic constitutive model considered here, we determine $\mathbb{P}(\mathbf{X}, t)$ from a strain energy function $W(\mathbb{F}(\mathbf{X}, t))$ by

$$\mathbb{P}(\mathbf{X}, t) = \frac{\partial W(\mathbb{F}(\mathbf{X}, t))}{\partial \mathbb{F}(\mathbf{X}, t)}.$$

Given that we consider the fluid to be Newtonian, then $\boldsymbol{\sigma}^f(\mathbf{x}, t)$ is

$$\boldsymbol{\sigma}^f(\mathbf{x}, t) = -p(\mathbf{x}, t)\mathbb{I} + \mu [\nabla \mathbf{u}(\mathbf{x}, t) + (\nabla \mathbf{u}(\mathbf{x}, t))^T].$$

Here, $\mathbf{u}(\mathbf{x}, t)$ represents the Eulerian velocity field, and $p(\mathbf{x}, t)$ represents the pressure field, which also acts as the Eulerian Lagrange multiplier to enforce the incompressibility constraint $\nabla \cdot \mathbf{u} = 0$, \mathbb{I} denotes the identity tensor, and μ is the dynamic viscosity.

Eulerian and Lagrangian variables are coupled through integral transforms with delta function kernels in the IB framework. Let $\delta(\mathbf{x}) = \prod_{i=1}^d \delta(x_i)$ denote the d -dimensional delta function, where x_i are the Cartesian components of the vector \mathbf{x} .^{23,24} Let $\mathbf{f}(\mathbf{x}, t)$ be the Eulerian elastic force density, $\mathbf{F}(\mathbf{X}, t)$ be the Lagrangian elastic force density, and $\mathbf{U}(\mathbf{X}, t)$ be the Lagrangian velocity field. Based on the definitions of the interpolation operator $\mathcal{J}(\cdot, \cdot)$ and spreading operator $\mathcal{E}(\cdot, \cdot)$ provided in,²⁵ we establish the relationships between $\mathbf{F}(\mathbf{X}, t)$ and $\mathbf{f}(\mathbf{x}, t)$, as well as $\mathbf{u}(\mathbf{x}, t)$ and $\mathbf{U}(\mathbf{X}, t)$ as follows:

$$\mathbf{f}(\mathbf{x}, t) = \mathcal{E}(\mathcal{X}, \mathbf{F}) = \int_{B_r} \mathbf{F}(\mathbf{X}, t) \delta(\mathbf{x} - \mathcal{X}(\mathbf{X}, t)) d\mathbf{X}, \quad (1)$$

$$\mathbf{U}(\mathbf{X}, t) = \mathcal{J}(\mathcal{X}, \mathbf{u}) = \int_{\Omega} \mathbf{u}(\mathbf{x}, t) \delta(\mathbf{x} - \mathcal{X}(\mathbf{X}, t)) d\mathbf{x}. \quad (2)$$

The present study is based on the IB method derived by Boffi et al.,¹⁰ find $\mathbf{u}(\mathbf{x}, t)$, $p(\mathbf{x}, t)$, $\mathcal{X}(\mathbf{X}, t)$ which satisfy

$$\rho \frac{D\mathbf{u}}{Dt}(\mathbf{x}, t) + \nabla p(\mathbf{x}, t) - \mu \Delta \mathbf{u}(\mathbf{x}, t) = \mathbf{f}(\mathbf{x}, t), \quad (3a)$$

$$\nabla \cdot \mathbf{u}(\mathbf{x}, t) = 0, \quad (3b)$$

$$\int_{B_r} \mathbf{F}(\mathbf{X}, t) \cdot \mathbf{V}(\mathbf{X}) d\mathbf{X} = - \int_{B_r} \mathbb{P}(\mathbf{X}, t) : \nabla_{\mathbf{X}} \mathbf{V}(\mathbf{X}) d\mathbf{X}, \quad (3c)$$

$$\mathbf{f}(\mathbf{x}, t) = \mathcal{E}(\mathcal{X}(\mathbf{X}, t), \mathbf{F}(\mathbf{X}, t)), \quad (3d)$$

$$\frac{\partial \mathcal{X}(\mathbf{X}, t)}{\partial t} = \mathbf{U}(\mathbf{X}, t) = \mathcal{J}(\mathcal{X}(\mathbf{X}, t), \mathbf{u}(\mathbf{x}, t)), \quad (3e)$$

where ρ be the density of the FSI system. And imposed the initial and boundary conditions

$$\begin{cases} \mathbf{u}(\mathbf{x}, t) = \mathbf{w}(\mathbf{x}, t), & \text{in } \partial\Omega \times [0, T], \\ \mathbf{u}(\mathbf{x}, 0) = \mathbf{u}_0(\mathbf{x}), & \text{in } \Omega. \end{cases} \quad (4)$$

Here, $\frac{D\mathbf{u}}{Dt}(\mathbf{x}, t) = \frac{\partial \mathbf{u}}{\partial t}(\mathbf{x}, t) + (\mathbf{u}(\mathbf{x}, t) \cdot \nabla) \mathbf{u}(\mathbf{x}, t)$, $\mathbf{V}(\mathbf{X})$ is any smooth function.

2.2 Constitutive laws

The Cauchy stress of the immersed elastic structure is decomposed in the traditional IB method as:^{10,11,26}

$$\boldsymbol{\sigma} = \boldsymbol{\sigma}^\nu - p\mathbb{1} + \begin{cases} 0, & \mathbf{x} \in \Omega_t^f, \\ \boldsymbol{\sigma}^e, & \mathbf{x} \in \Omega_t^s. \end{cases} \quad (5)$$

where $\boldsymbol{\sigma}^\nu = \mu(\nabla\mathbf{v} + \nabla\mathbf{v}^T)$ is the deviatoric viscous stress and $\boldsymbol{\sigma}^e$ is the elastic stress. To address the poor numerical results¹² that may arise from Eq. (5), $\boldsymbol{\sigma}^e$ is decomposed as:

$$\boldsymbol{\sigma}^e = \text{dev}[\boldsymbol{\sigma}^e] - \pi_{\text{stab}}\mathbb{1},$$

where $\text{dev}[\boldsymbol{\sigma}^e]$ represents the deviatoric stress component, and $\pi_{\text{stab}}\mathbb{1}$ represents the volumetric stress component, which serves as a stabilization term that acts like an additional pressure in solid region. Based on,¹² π_{stab} depends on the volumetric energy $U(J)$, which is solely related to the volume changes of the structure.

$$\pi_{\text{stab}} = -\frac{\partial U(J)}{\partial J}.$$

In this paper, a simple form of $U(J)$ is chosen as $U(J) = \frac{\kappa_{\text{stab}}}{2}(\ln J)^2$, where the value of κ_{stab} depends on the numerical Poisson ratio ν_{stab} , and $\kappa_{\text{stab}} = \frac{2G_T(1+\nu_{\text{stab}})}{3(1-2\nu_{\text{stab}})}$. Thus, for hyperelastic materials, based on $\boldsymbol{\sigma}^e = \frac{1}{J} \frac{\partial \Psi(\mathbb{F})}{\partial \mathbb{F}} \mathbb{F}^T$, it follows that:

$$\Psi(\mathbb{F}) = W(\mathbb{F}) + U(J),$$

where $W(\mathbb{F})$ is the volume-preserving components, $U(J)$ is the volume-changing component.

To ensure material frame invariance, this study considers anisotropic materials and, based on,^{12,27} defines their strain energy function Ψ in the following general form using the right Cauchy-Green tensor $\mathbb{C} = \mathbb{F}^T \mathbb{F}$:

$$\Psi = W(I_1, I_{4f}, I_{4s}, I_{5f}, I_{8fs}) + U(J),$$

where $I_1 = \text{tr}(\mathbb{C})$, $I_{4f} = \mathbf{e}_f \cdot (\mathbb{C}\mathbf{e}_f)$, $I_{5f} = \mathbf{e}_f \cdot (\mathbb{C}^2\mathbf{e}_f)$, $I_{4s} = \mathbf{e}_s \cdot (\mathbb{C}\mathbf{e}_s)$, $I_{8fs} = \mathbf{e}_f \cdot (\mathbb{C}\mathbf{e}_s)$, \mathbf{e}_f represents the fiber direction in the reference configuration, and \mathbf{e}_s represents the sheet direction in the reference configuration.

Next, to remove volume change information, the material used in this study introduces modified invariants based on I_1 , as follows:

$$\bar{I}_1 = J^{-2/3} I_1.$$

Therefore, the Ψ represented by the modified invariant \bar{I}_1 is:

$$\Psi = \bar{W}(\bar{I}_1, I_{4f}, I_{4s}, I_{5f}, I_{8fs}) + U(J).$$

Finally, we will briefly introduce several common constitutive models, including their free energy functions and the corresponding first Piola-Kirchhoff stress tensors.

- Modified standard reinforcing model:¹²

$$\begin{aligned} \Psi_1 &= \frac{G_T}{2}(\bar{I}_1 - 3) + \frac{G_T - G_L}{2}(2I_{4f} - I_{5f} - 1) \\ &\quad + \frac{E_L + G_T - 4G_L}{8}(I_{4f} - 1)^2 + \frac{\kappa_{\text{stab}}}{2}(\ln J)^2, \end{aligned} \quad (6)$$

$$\begin{aligned} \mathbb{P}_1 &= G_T J^{-2/3} (\mathbb{F} - \frac{I_1}{3} \mathbb{F}^{-T}) + (G_T - G_L)(2\mathbb{F}\mathbf{e}_f \otimes \mathbf{e}_f - \mathbb{F}\mathbf{e}_f \otimes \mathbf{e}_f \mathbb{C} - \mathbb{F}\mathbb{C}\mathbf{e}_f \otimes \mathbf{e}_f) \\ &\quad + \frac{E_L + G_T - 4G_L}{2}(I_{4f} - 1)\mathbb{F}\mathbf{e}_f \otimes \mathbf{e}_f + \kappa_{\text{stab}} \ln(J)\mathbb{F}^{-T}, \end{aligned} \quad (7)$$

where G_T , G_L , E_L are material constants.

- Fiber-reinforced hyperelastic model 1:²⁸

$$\Psi_2 = C_1(\bar{I}_1 - 3) + \frac{a_f}{2b_f} \left(\exp \left[b_f(I_{4f}^* - 1)^2 \right] - 1 \right) + \frac{\kappa_{\text{stab}}}{2} (\ln J)^2, \quad (8)$$

$$\mathbb{P}_2 = 2C_1 J^{-2/3} \left(\mathbb{F} - \frac{I_1}{3} \mathbb{F}^{-T} \right) + 2a_f(I_{4f}^* - 1) \exp \left[b_f(I_{4f}^* - 1)^2 \right] \mathbb{F} \mathbf{e}_f \otimes \mathbf{e}_f + \kappa_{\text{stab}} \ln(J) \mathbb{F}^{-T}, \quad (9)$$

where $I_{4f}^* = \max(I_{4f}, 1)$, C_1 , a_f , b_f are the material constants.

- Fiber-reinforced hyperelastic model 2:²⁹

$$\Psi_3 = C_{10} \left(\exp \left[C_{01}(\bar{I}_1 - 3) \right] - 1 \right) + \frac{a_f}{2b_f} \left(\exp \left[b_f(I_{4f} - 1)^2 \right] - 1 \right) + \frac{\kappa_{\text{stab}}}{2} (\ln J)^2, \quad (10)$$

$$\mathbb{P}_3 = 2C_{10}C_{01} \exp \left[C_{01}(\bar{I}_1 - 3) \right] J^{-2/3} \left(\mathbb{F} - \frac{I_1}{3} \mathbb{F}^{-T} \right) + 2a_f(I_{4f} - 1) \exp \left[b_f(I_{4f} - 1)^2 \right] \mathbb{F} \mathbf{e}_f \otimes \mathbf{e}_f + \kappa_{\text{stab}} \ln(J) \mathbb{F}^{-T}, \quad (11)$$

where C_{10} , C_{01} , a_f , b_f are the material constants.

- Holzapfel-Ogden (HO) model:³⁰

$$\begin{aligned} \Psi_4 &= \frac{a}{2b} \exp[b(\bar{I}_1 - 3)] + \sum_{i=f,s} \frac{a_i}{2b_i} \left\{ \exp \left[b_i(I_{4i}^* - 1)^2 \right] - 1 \right\} \\ &\quad + \frac{a_{fs}}{2b_{fs}} \left\{ \exp \left[b_{fs}(I_{8fs})^2 \right] - 1 \right\} + \frac{\kappa_{\text{stab}}}{2} (\ln J)^2, \end{aligned} \quad (12)$$

$$\begin{aligned} \mathbb{P}_4 &= a \exp \left[b(\bar{I}_1 - 3) \right] J^{-2/3} \left(\mathbb{F} - \frac{I_1}{3} \mathbb{F}^T \right) + \sum_{i=f,s} 2a_i(I_{4i}^* - 1) \exp \left[b_i(I_{4i}^* - 1)^2 \right] \mathbb{F} \mathbf{e}_i \otimes \mathbf{e}_i \\ &\quad + 2a_{fs}I_{8fs} \exp \left[b_{fs}(I_{8fs})^2 \right] \mathbb{F} \mathbf{e}_f \otimes \mathbf{e}_s + \kappa_{\text{stab}} \ln(J) \mathbb{F}^{-T}, \end{aligned} \quad (13)$$

where $I_{4i}^* = \max(I_{4i}, 1)$, a , b , a_i , b_i , a_{fs} , and b_{fs} are material constants, with $i = f, s$.

3 Numerical Discretization

3.1 Temporal discretization

We begin by considering the temporal semi-discretization for system (3). The time interval $[0, T]$ is partitioned into N uniformly spaced, non-overlapping subintervals $(t_n, t_{n+1}]$, where $n = 1, 2, \dots, N$, with a constant time step size $t_{n+1} - t_n = \Delta t$. Here, $(\cdot)^n$ denotes the value of (\cdot) at time t_n . In this work, the modified backward Euler time-stepping scheme is employed for the temporal discretization,²⁵ and the resulting semi-discrete system is given as follows:

$$\rho \left(\frac{\mathbf{u}^{n+1} - \mathbf{u}^n}{\Delta t} + \mathbf{u}^n \cdot \nabla \mathbf{u}^n \right) = \mu \Delta \mathbf{u}^{n+1} - \nabla p^{n+1} + \mathbf{f}^n, \quad (14a)$$

$$\nabla \cdot \mathbf{u}^{n+1} = 0, \quad (14b)$$

$$\int_{B_r} \mathbf{F}^n \cdot \mathbf{V}(\mathbf{X}) d\mathbf{X} = - \int_{B_r} \mathbb{P}^n : \nabla_{\mathbf{X}} \mathbf{V}(\mathbf{X}) d\mathbf{X}, \quad (14c)$$

$$\mathbf{f}^n = \mathcal{E}(\mathcal{X}^n, \mathbf{F}^n), \quad (14d)$$

$$\mathcal{X}^{n+1} = \mathcal{X}^n + \Delta t \mathcal{J}(\mathcal{X}^n, \mathbf{u}^n). \quad (14e)$$

Eq (14) employs an explicit coupling strategy for FSI problems, where the force term \mathbf{f}_n depends only on physical quantities at time t_n . Although many implicit time-stepping methods have been proposed,^{31,32} which allow significantly

larger time steps, their implementation on GPUs remains challenging due to the need to solve large, nonlinear systems. As a result, explicit coupling methods are still widely used in large-scale numerical simulations for their simplicity and computational efficiency. In this work, we therefore adopt an explicit scheme as the foundation for the fully GPU-accelerated algorithm.

3.2 Spatial discretization

In the spatial discretization, we adopt the staggered-grid marker and cell approach for the Eulerian domain, following the approach of,^{11,21} to approximate the Eulerian variables defined in the incompressible Navier-Stokes equations. Taking the three-dimensional space as an example, the computational domain Ω is discretized into uniform grid cells, where the cell length in each coordinate direction (x, y, z) is h , forming a structured grid system. Eulerian variables, including pressure p , velocity $\mathbf{u} = (u^1, u^2, u^3)$, and force $\mathbf{f} = (f^1, f^2, f^3)$, are defined on a staggered grid, as shown in Fig. 1. Specifically, the pressure p is located at the cell center, while the velocity components u^1, u^2 , and u^3 are positioned at the centers of the cell faces perpendicular to the x, y , and z axes, respectively. The force components f^1, f^2 , and f^3 are collocated with the corresponding velocity components. This staggered grid arrangement effectively enhances computational accuracy in the IB method.

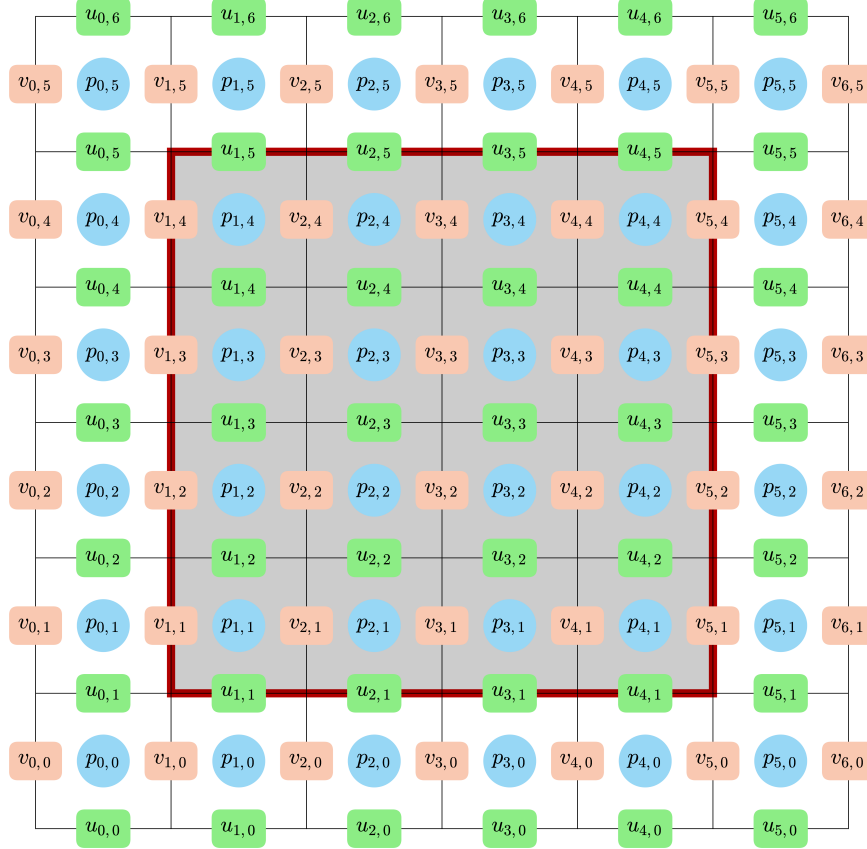


Figure 1: Schematic diagram of the staggered grid arrangement of Eulerian variables in the xy -plane within a three-dimensional space.

For the Lagrangian domain, let \mathcal{T}_h be a consistent triangulation of B_r in a finite number of simplices, where \mathcal{T}_h consists of m nodes for FE basis, and define a $3m$ -dimensional vector-valued approximation space as V_h . Notably, m is larger than mesh nodes as shown in Fig. ?? . Let $\{\phi_l\}$ be the standard primitive (i.e., nonzero in exactly one component) nodally interpolating finite element basis of \mathbf{V}^h . Consequently, for each node \mathbf{X}_k of Γ^h there are exactly three basis functions that are nonzero at that node. For example, $k, m+k$, and $2m+k$ are the unique indices such that

$$\phi_k(\mathbf{X}_k) = (1, 0, 0), \quad \phi_{m+k}(\mathbf{X}_k) = (0, 1, 0), \quad \phi_{2m+k}(\mathbf{X}_k) = (0, 0, 1),$$

and otherwise $\phi_i(\mathbf{X}_k) = (0, 0, 0)$ for $i \neq k$, $i \neq m + k$, and $i \neq 2m + k$.

The deformation \mathcal{X} , velocity \mathbf{U} , and force \mathbf{F} are all approximated in \mathbf{V}^h can be written as **ignore the t in \mathcal{X} , \mathbf{U} and \mathbf{F} for the convenience of notation**

$$\begin{aligned}\mathcal{X}_h(\mathbf{X}, t) &= \sum_{l=1}^{3m} \mathcal{X}_l(t) \phi_l(\mathbf{X}), \\ \mathbf{U}_h(\mathbf{X}, t) &= \sum_{l=1}^{3m} U_l(t) \phi_l(\mathbf{X}), \\ \mathbf{F}_h(\mathbf{X}, t) &= \sum_{l=1}^{3m} F_l(t) \phi_l(\mathbf{X}),\end{aligned}$$

Because each basis function is nonzero in only one component, for convenience we also define \mathbf{U}_h^n and \mathbf{F} for $1 \geq n \geq 3$ as the n th components of each finite element field, whose basis functions are indexed in the same order as the mesh nodes (e.g., U_k^1 is the x -component of the finite element velocity at mesh node \mathbf{X}_k).

3.3 Discretization for Eulerian-Lagrangian coupling operators

This subsection focuses on the discretization of Eq. (14c), (14d) and (14e). The IB-4 delta function proposed by Peskin²³ as the regularized delta function δ_h is used. We use the nodal quadrature rule and the higher-order quadrature rule as the notations in:²¹ $\mathbf{F}(\mathbf{X}_q)$ can be evaluated as the freedom of the finite element basis function $\phi_q(\mathbf{X})$.

- The nodal quadrature rule is

$$\mathbb{N}_q = \{(\mathbf{X}_q, w_q)\}_{q=1}^m, \quad (15)$$

where $\phi_q(\mathbf{X})$ is the basis function associated with node \mathbf{X}_q , \mathbf{X}_q is the node for corresponding basis function, $w_q = \int \phi_q(\mathbf{X}) \cdot \mathbf{1} d\mathbf{X}$ is the integration weight and m is 4 for first order element and m is 10 for second order element. The approximation of the left part of Eq. (14c) can be written as

$$\sum_{(\mathbf{X}_q, w_q) \in \mathbb{N}_q} \mathbf{F}_h(\mathbf{X}_q) \phi_q(\mathbf{X}_q) \phi_j(\mathbf{X}_q) w_q \approx \int_{B_r} \mathbf{F} \cdot \phi_j(\mathbf{X}) d\mathbf{X} \quad (16)$$

- The higher-order quadrature rule

$$\mathbb{H}_q = \{(\mathbf{X}_q, w_q)\}_{q=1}^m, \quad (17)$$

where m is decided by the complexity of constitutive law in our paper we choose 7th order quadrature rule where the m is equal to 64 in our paper. The approximation of the right part of Eq. (14c) can be written as

$$\sum_{(\mathbf{X}_q, w_q) \in \mathbb{H}_q} -\mathbb{P}^e(\mathcal{X}_h(\mathbf{X}_q, t)) : \nabla_{\mathbf{X}} \phi_j(\mathbf{X}_q) w_q \approx - \int_{B_r} \mathbb{P}^e(\mathbf{X}, t) : \nabla_{\mathbf{X}} \phi_j(\mathbf{X}) d\mathbf{X}, \quad \forall \phi_j \in \mathbf{V}^h.$$

Next, apply (15) and (17) to discretize Eq. (14c), (14d) and (14e). As in,²¹ there is no need to calculate w_q in \mathbb{N}_q during the assembly process and distribution. Define \hat{F}_i as the contribution of each basis function. Using the high-order integration rule, compute \hat{F}_i as follows:

$$\hat{F}_i = - \sum_{(\mathbf{X}_q, w_q) \in \mathbb{H}_q} \mathbb{P}^e(\mathbf{X}_q) : \nabla_{\mathbf{X}} \phi_i(\mathbf{X}_q) w_q, \quad (18)$$

then \hat{F}_i is transferred from the structural mesh to the Cartesian grid by δ_h and the node displacement $\mathcal{X}_h(\mathbf{X}_q)$ as follows:

$$\begin{aligned} f_{i+\frac{1}{2},j,k}^1 &= \sum_{(\mathbf{X}_q, w_q \in \mathbb{N}_q)} F_q^1 \delta_h(\mathbf{x}_{i+\frac{1}{2},j,k} - \mathcal{X}_h(\mathbf{X}_q)) \\ f_{i,j+\frac{1}{2},k}^2 &= \sum_{(\mathbf{X}_q, w_q \in \mathbb{N}_q)} F_q^2 \delta_h(\mathbf{x}_{i,j+\frac{1}{2},k} - \mathcal{X}_h(\mathbf{X}_q)) \\ f_{i,j,k+\frac{1}{2}}^3 &= \sum_{(\mathbf{X}_q, w_q \in \mathbb{N}_q)} F_q^3 \delta_h(\mathbf{x}_{i,j,k+\frac{1}{2}} - \mathcal{X}_h(\mathbf{X}_q)) \end{aligned}$$

where $\mathbf{f}_h^{n+1} = (f^{n+1,1}, f^{n+1,2}, f^{n+1,3})$. notably weight w_q is also not used in the above equation. Define $\mathbf{U}_q^{n+1} = (U_q^{n+1,1}, U_q^{n+1,2}, U_q^{n+1,3})$ as the value of \mathbf{U}^{n+1} at the nodes. For any $\mathbf{X}_q, w_q \in \mathbb{N}_q$, the velocity \mathbf{u}_h^n is transferred from the Cartesian grid to the structural mesh by δ_h and the node displacement $\mathcal{X}_h(\mathbf{X}_q)$, as follows:

$$\begin{aligned} U_q^{n+1,1} &= \sum_{i,j,k} u_{i+\frac{1}{2},j,k}^1 \delta_h(\mathbf{x}_{i+\frac{1}{2},j,k} - \mathcal{X}_h(\mathbf{X}_q)) h^3, \\ U_q^{n+1,2} &= \sum_{i,j,k} u_{i,j+\frac{1}{2},k}^2 \delta_h(\mathbf{x}_{i,j+\frac{1}{2},k} - \mathcal{X}_h(\mathbf{X}_q)) h^3, \\ U_q^{n+1,3} &= \sum_{i,j,k} u_{i,j,k+\frac{1}{2}}^3 \delta_h(\mathbf{x}_{i,j,k+\frac{1}{2}} - \mathcal{X}_h(\mathbf{X}_q)) h^3. \end{aligned} \quad (19)$$

The duality and accuracy of the discretization above are discussed in.²¹

3.4 Algorithm

We first discuss the computational methods for the fluid and solid solvers on the GPU, followed by the complete fluid-structure interaction algorithm.

Solver for Navier-Stokes equations: In the numerical solution of Eqs. (14a) and (14b), we first decompose the equations using Chorin's projection method and the semi-Lagrangian method, as shown below:

$$\hat{\mathbf{u}}_h^n = \mathbf{u}_h(\mathbf{x} - \Delta t \mathbf{u}_h^n, t) \quad (20)$$

$$\frac{\rho}{\Delta t} (\mathbf{u}_h^* - \hat{\mathbf{u}}_h^n) - \mu \Delta_h \mathbf{u}_h^* = \mathbf{f}^n, \quad (21)$$

$$\Delta_h p_h^{n+1} = \frac{1}{\Delta t} \nabla_h \cdot \mathbf{u}_h^*, \quad (22)$$

$$\mathbf{u}_h^{n+1} = \mathbf{u}_h^* - \Delta t \nabla_h p_h^{n+1}. \quad (23)$$

Here, Eq. (20) represents the advective term solved using a semi-Lagrangian approach, and Eq. (21) corresponds to a Helmholtz equation. The pressure correction in Eq. (22) is formulated as a Poisson equation, and Eq. (23) completes the velocity update.

To address boundary condition issues and avoid warp divergence on the GPU, we express the original variable as $u = u' + u''$, where u' is a constructed function satisfying the boundary conditions. Substituting $u = u' + u''$ into the original equations yields an equation for u'' , which satisfies homogeneous Neumann or Dirichlet boundary conditions, thereby simplifying the numerical treatment of boundaries.

For parallel computation, in order to ensure consistency with serial solver results, we employ the red-black Gauss-Seidel iteration as the internal iterative strategy. Specifically, for the Helmholtz equation in Eq.,(21), because the time step is sufficiently small, we use the solution from the previous time step as the initial guess and directly apply the red-black Gauss-Seidel iteration, which typically converges within a few steps. For the Poisson equation (22), we combine multigrid methods with red-black Gauss-Seidel iteration as smoother to accelerate convergence. Moreover, given the sufficiently small time step, the semi-Lagrangian method effectively controls error propagation in practice. By leveraging texture memory to accelerate data access, the method also helps reduce global memory access latency.

Solver for structural force: To efficiently compute structural forces Eq. (18), we leverage key feature of constant memory provided on GPU hardware level, which is single-cycle broadcast. During the initialization, the values and derivatives of basis functions on quadrature points are precomputed and stored in constant memory. This allocation uses $(1+3) \times 64 \times 10 \times 8B = 20KB$ of constant memory, with 64 quadrature points, 10 basis functions, and double precision, providing 7th order of quadrature accuracy. Constitutive parameters are also loaded into constant memory. These values are well within the GPU's 64KB constant memory limit.

Additionally, we precompute the inverse of the Jacobian matrix for each element, which maps points from the local element to the reference element. we precompute as well as the local element volume. We also iterate over the elements to store the degree-of-freedom map (dofmap) for every element, which is 10 integral values per element. Considering the sheet and fiber directions in fiber-reinforced materials, the memory footprint per element is approximately $(3 \times 3 + 1 + 3 + 3) \times 8B + 10 \times 4B = 168B$. While our strategy increases memory consumption, it significantly accelerates computation.

The displacements $\hat{X}_h(t)$, the initial positions $\hat{X}_h(0)$ (for tethering), along with the resulting structural forces $\hat{F}_h(t)$ of the structure, are stored in a global vector as coefficients of the basis functions. The coefficients associated with each element are accessible via the degree-of-freedom map (dofmap).

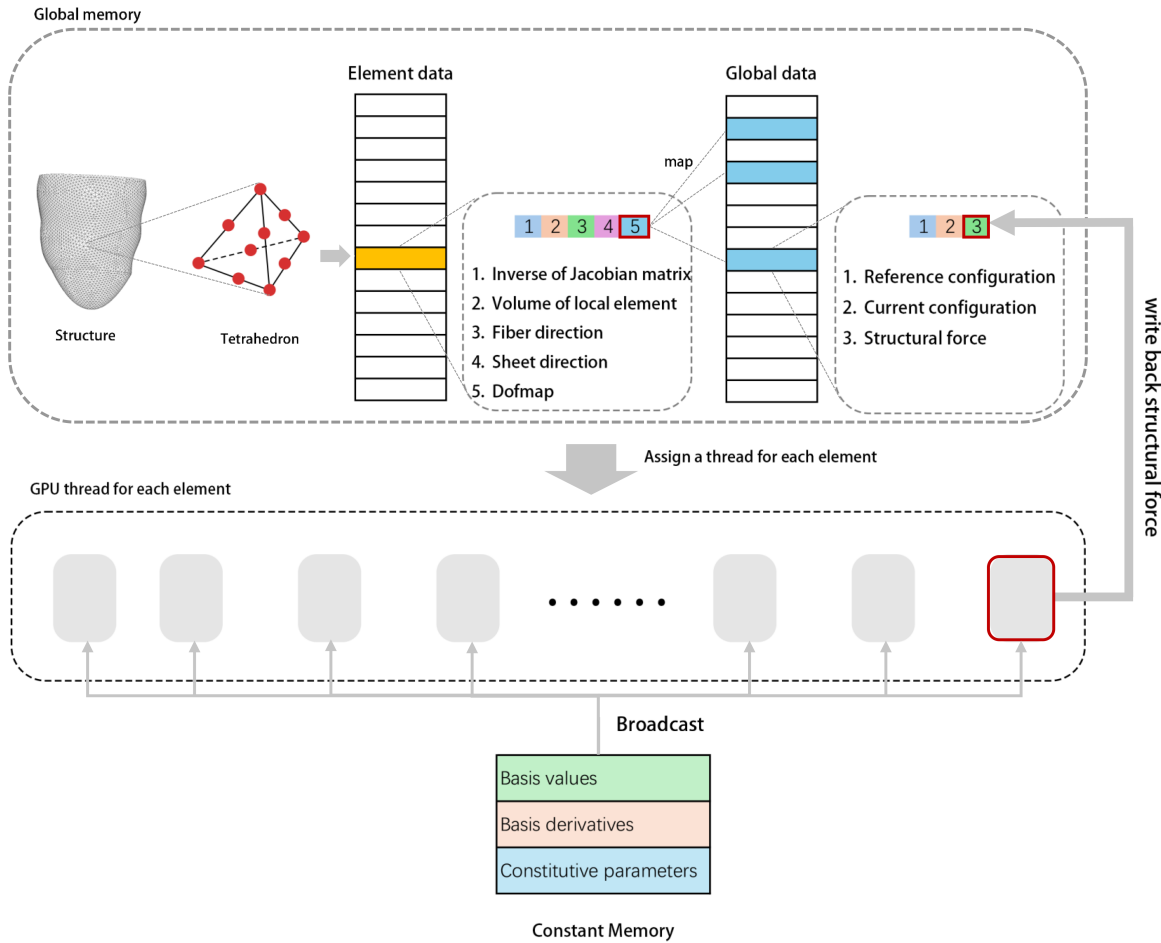


Figure 2: Setup of the anisotropic Cook's membrane benchmark: The gray region represents the fixed computational domain Ω , while the red region corresponds to the deformable structure.

In our implementation, the force vector assembly is carefully optimized:

- **Element indexing:** For each element, we gather information from the dofmap, fiber directions, the inverse Jacobian, and the element volume.
- **Data retrieval:** After reading the dofmap, we retrieve the initial positions, displacements, and reset the structural

force accumulator.

- **Nodal force computation:** Structural forces are computed per element and then written back to the global force array using the dofmap. To safely accumulate contributions into the global force vector, we use atomic operations to avoid race conditions during parallel writes.

The strategic use of constant memory, combined with these optimization techniques, results in significant performance improvements for the structural solver on the GPU.

Fluid-Structure Coupling: A staggered algorithm is used in our study which permit independent solving of the fluid and solid systems. For both operators, to keep the complexity of $O(m)$, we need to iterate nodal, Key steps in the coupling process are:

1. **Structural Force Solver.** Solve the structural force in the Lagrangian description: $\mathcal{X}^n \rightarrow \mathbf{F}_h^n$;
2. **Lagrangian to Eulerian.** Distribute the structural force onto the Eulerian grid: $\mathbf{F}^n \rightarrow \mathbf{f}_h^n$;
3. **Navier-Stokes Solver.** Solve the velocity in the Eulerian description: $\{\mathbf{u}^n, \mathbf{f}^n\} \rightarrow \{\mathbf{u}^{n+1}, \mathbf{f}^{n+1}\}$;
4. **Eulerian to Lagrangian.** Interpolate the velocity into the Lagrangian mesh and update its current configuration: $\mathbf{u}^{n+1} \rightarrow \mathcal{X}_h^{n+1}$.

The process is illustrated in Fig. 2. The solid solver is executed first In summary, the algorithm utilizes GPU

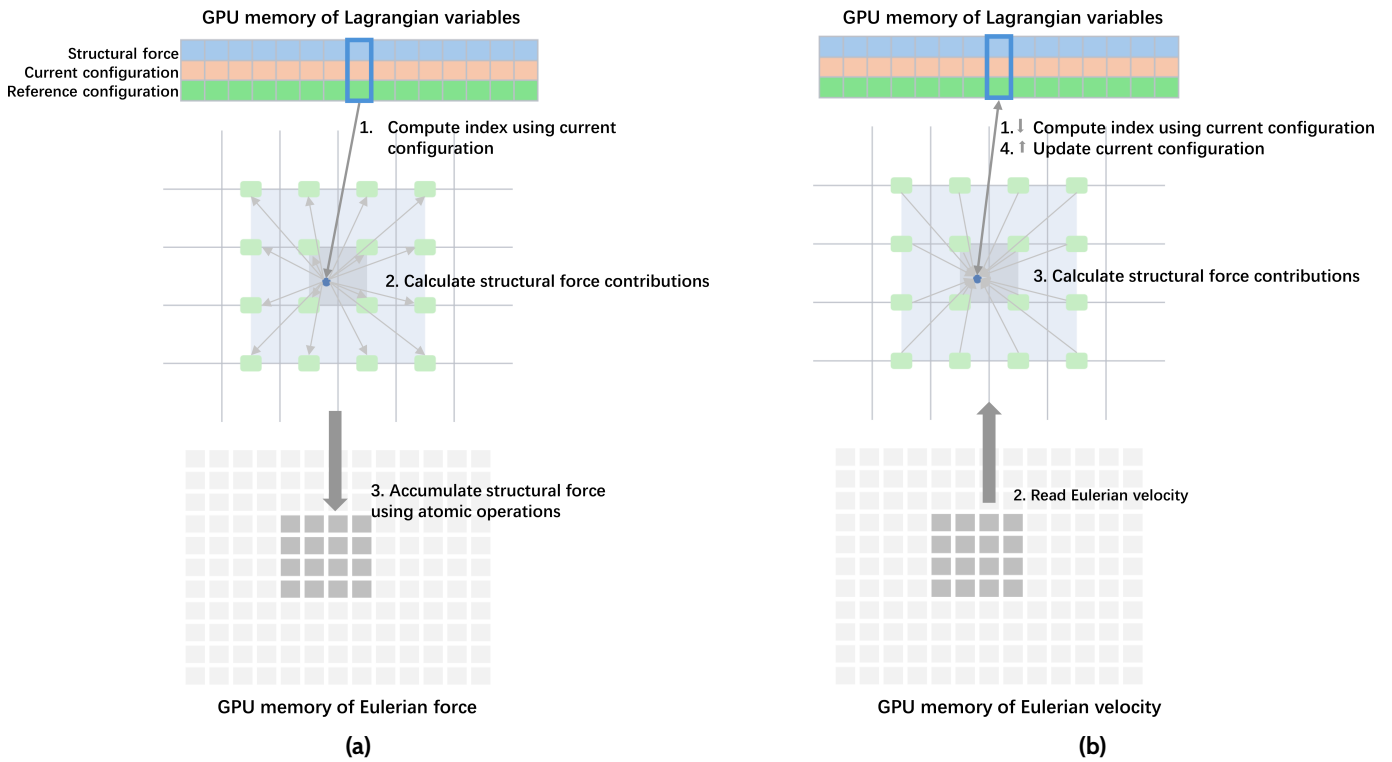


Figure 3: (a) Schematic diagram of the staggered grid arrangement of Eulerian variables in the xy-plane within a three-dimensional space. (b) Coordinates associated with degrees of freedom of the unstructured tetrahedron.

optimizations, including texture memory, constant memory for basis functions, and efficient iterative solvers like red-black Gauss-Seidel with multigrid acceleration. These techniques together create a robust and efficient fluid-structure coupling framework, ideal for high-fidelity simulations of complex cardiac models.

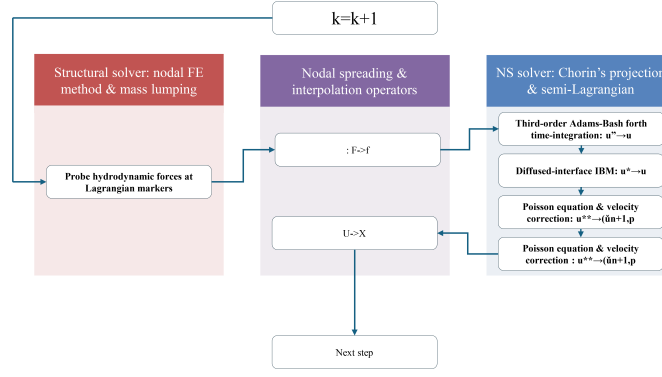


Figure 4: Setup of the anisotropic Cook’s membrane benchmark: The gray region represents the fixed computational domain Ω , while the red region corresponds to the deformable structure.

3.5 Computational devices

We perform simulations primarily on a GeForce RTX 4090 GPU, with additional tests on NVIDIA V100 and P100 GPUs for comparison. CPU-based simulations using IBAMR of version 0.5.1 run on a dual Intel Xeon 5115 workstation (10 cores per CPU). Notably, the RTX 4090 is a consumer-grade GPU with limited double-precision performance (1/64 of single-precision) and restricted multi-GPU capabilities, but at a fraction of the cost of professional cards, making it highly suitable for practical applications. Our results show the RTX 4090 is fully adequate for our simulations, and we expect future GPU advances to further improve our framework’s ability to handle complex cardiac models.

4 Benchmark Problem

4.1 Cook’s Membrane Benchmark

The Cook’s membrane problem is a classical benchmark in incompressible elastic solid mechanics. To assess the computational performance of the fully GPU-implemented IB method, we follow the setup in¹² to embed the three-dimensional anisotropic Cook’s membrane into an incompressible Newtonian fluid, formulating a fluid-structure interaction system, which is then numerically solved using the IB method. The configuration of the computational domain Ω , structural dimensions, and loading conditions is shown in Fig. 5.

The boundary conditions for this problem consist of a fixed left face, where constraints are enforced using a penalty parameter of $\kappa = 10^6$. A vertical traction of $6.25 \frac{\text{dyn}}{\text{cm}^2}$ is applied to the right face, increasing gradually according to the polynomial function $q(t) = -2(\frac{t}{T_1})^3 + 3(\frac{t}{T_1})^2$ and reaching its maximum at time T_1 . The simulation continues until time T_f to ensure the system reaches equilibrium. All other faces are subject to zero traction conditions. A summary of the relevant physical and numerical parameters is provided in Table 1.

In this case, the computational domain Ω is discretized using a Cartesian grid comprising $N = 64$ cells along each coordinate axis. A tetrahedral mesh is utilized for the discretization of the structure, and the forces and displacements are discretized using $P2$ finite elements. The degrees of freedom (DoFs) for the solid range from $m = 5004$ to $m = 282,489$. Furthermore, the time step for the simulation is set to $\Delta t = 0.001\text{s}$.

To verify the accuracy of our computational results, we primarily focus on the deformation of the Cook’s membrane, the determinant of the element Jacobian matrix (J), and the vertical displacement at the upper right corner $A = (7.06 \text{ cm}, 8.0 \text{ cm}, 4.5 \text{ cm})$ of the membrane. Fig. 6 illustrates the deformation of the Cook membrane at the final time from different angles. The results appear to be consistent with those in¹² Fig. 7a presents the computational results for J . Upon examining the figure, it is clear that J is uniformly close to 1 throughout the entire solid. Fig. 7b compares the volume change rates of solids calculated by our method under various degrees of freedom with those reported in¹² The analysis reveals that the volume change rates derived from our calculations range from -0.00062% to -0.0088% , closely aligning with the data presented in¹² Of particular note, the results obtained using $P2$ elements in our study

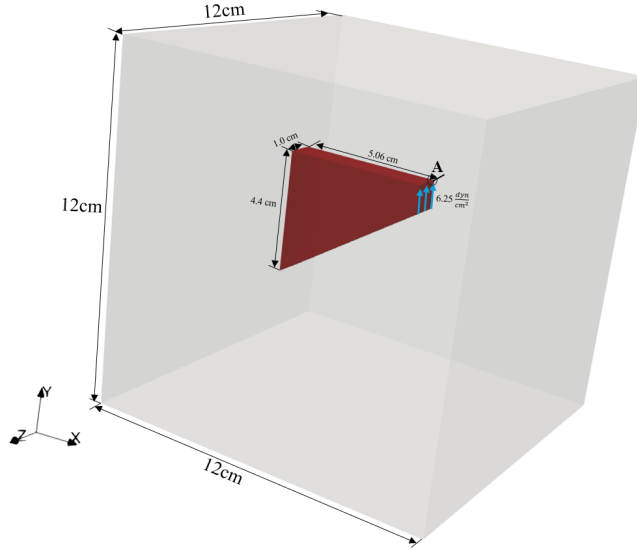


Figure 5: Setup of the anisotropic Cook’s membrane benchmark: The gray region represents the fixed computational domain Ω , while the red region corresponds to the deformable structure.

Symbol	Value	Unit
ρ	1.0	$\frac{\text{g}}{\text{cm}^3}$
T_1	14	s
T_f	35	s
μ	0.16	$\frac{\text{dyn}\cdot\text{s}}{\text{cm}^2}$
G_T	8.0	$\frac{\text{dyn}}{\text{cm}^2}$
G_L	160.0	$\frac{\text{dyn}}{\text{cm}^2}$
E_L	1200.0	$\frac{\text{dyn}}{\text{cm}^2}$
κ_{stab}	112	$\frac{\text{dyn}}{\text{cm}^2}$
\mathbf{e}_f	$\frac{1}{\sqrt{3}}(1, 1, 1)$	-

Table 1: Parameters for the anisotropic Cook’s membrane benchmark

are nearly identical to those calculated using $Q1$ elements as documented in.¹² Fig. 8a illustrates the variation of the displacement of point A along the y -axis over time. Fig. 8b shows the variation in the maximum displacement of point A along the y -axis with different Dofs of the solid. Furthermore, Fig. 8b demonstrates that the displacement of point A in the y -axis, as calculated by our method, is essentially consistent with the results reported in the literature.¹² All of these results substantiate the accuracy of our algorithm.

5 Cardiac Dynamics Applications

In this section, the fully GPU-parallelized IB method developed in this study is used to simulate several complex cardiac FSI problems, evaluating the algorithm’s applicability and generalizability across different cardiac structures. Cardiac FSI problems, due to their inherent geometric complexity and physical nonlinearity, place significant demands on

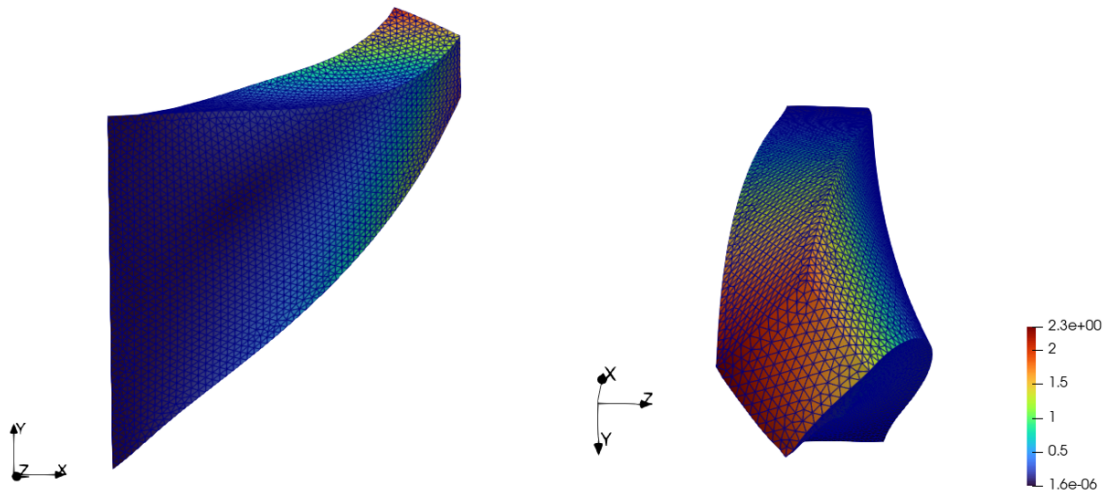


Figure 6: Deformations of the anisotropic Cook's membrane at different angles.

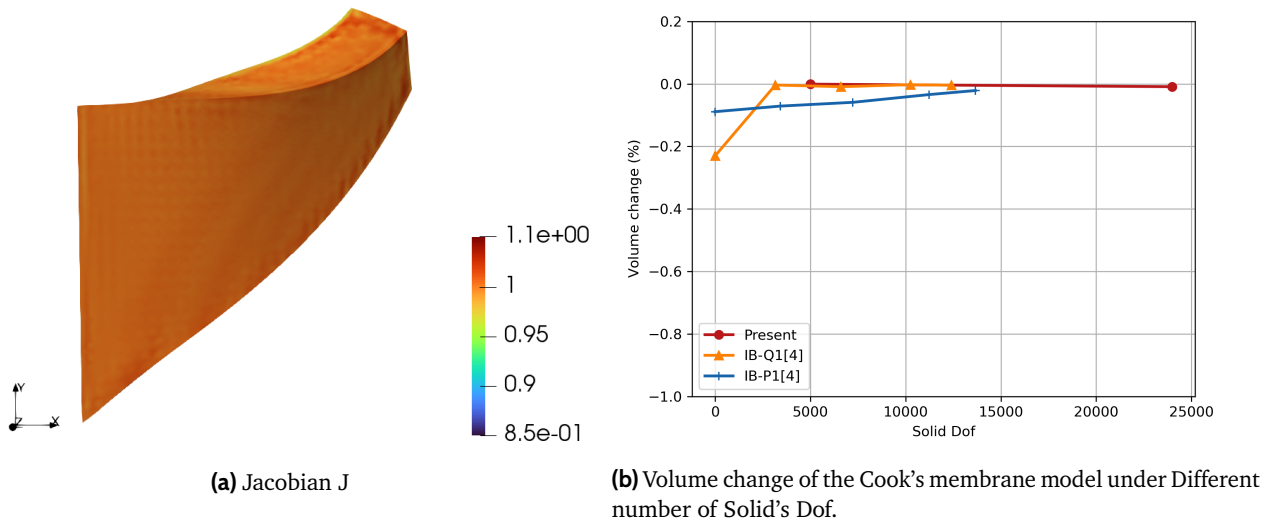
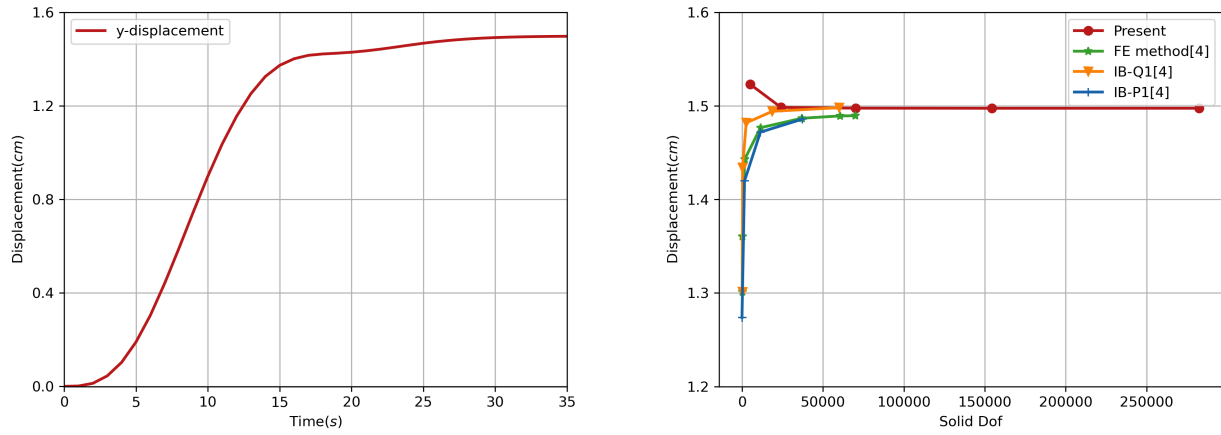


Figure 7: Volume conservation for the anisotropic Cook's membrane benchmark.

the accuracy and efficiency of computational methods. The selected benchmark cases include three representative models: the LV, the AV, and the MV, which correspond to strong FSI coupling between large myocardial deformation and intraventricular flow, high-speed flow through thin, flexible structures, and the simulation of complex valvular dynamic behavior, respectively. The simulation results validate the superior performance of the proposed method in terms of computational accuracy, efficiency, and numerical stability, while also revealing the mechanical response characteristics of key cardiac structures under typical physiological conditions. Furthermore, to further assess the method's accuracy, the results from all test cases are systematically compared with published reference data.

5.1 Dynamic left ventricle model

As one of the four chambers of the heart, the LV plays a crucial role in the heart's pumping function. This section is based on a previously developed image-based geometric model,³³ similar to many existing studies,^{3,34,35} considers only a portion of the LV (see Fig. 9) to investigate a simplified cardiac mechanics problem relevant to physiological conditions.



(a) Displacement of point A over time in a solid mesh with 282,489 Nodes and a fluid mesh divided into a $64 \times 64 \times 64$ grid. (b) Difference numbers of Dof on the displacement of Point A for the Cook's membrane model.

Figure 8: Corner y-displacement for the anisotropic Cook's membrane benchmark.

	CPU-GPU Heterogeneous		Full GPU (Present)	
	(%)	(s)	(%)	(s)
Fluid Solver (Poisson equation)	71.35	10827.8	72.4	659
Fluid Solver (Helmholtz equation)	26.99	4095.58	13.41	122
Fluid Solver (Convective Term)	0.34	51.59	0.15	1.339
Interpolation	1.25	189.31	0.42	3.804
Spreading	1.25	189.31	0.44	3.959
Solid Solver	1.25	189.31	8.68	79

Table 2: Execution time distribution of major algorithmic modules in the anisotropic Cook's membrane model under different parallelization strategies (CPU-GPU heterogeneous vs. fully GPU-parallel)

Solid Dof	CPU-GPU Heterogeneous(s)	Full GPU (Present) (s)	Speedup
5004		910	
23991		904	
70161		910	
154374		1003	
282489		1017	

Table 3: Full GPU parallel vs. CPU-GPU Interaction parallel: speedup comparison for different solid DoFs in solving the anisotropic Cook's membrane model.

In the LV model shown in Fig. 9, zero normal and circumferential displacements are applied at the base, allowing only radial expansion within the plane of the base. Meanwhile, the internal blood pressure is modeled by a uniform

pressure applied to the endocardial surface, varying according to the prescribed waveform $p_{\text{endo}}(t)$ as referenced in.³⁰ The maximum endocardial pressures during diastole and systole are 1067 Pa and 14530 Pa, respectively, as defined below.

$$p_{\text{endo}}(t) = \begin{cases} \frac{1067t}{0.2} \text{ Pa}, & \text{if } t < 0.2, \\ 1067 \text{ Pa}, & \text{if } 0.2 < t < 0.5, \\ 1067 + 13460 \left(1 - \exp\left(-\frac{(t-0.5)^2}{0.004}\right)\right) \text{ Pa}, & \text{if } 0.5 < t < 0.65, \\ 1067 + 13460 \left(1 - \exp\left(-\frac{(0.8-t)^2}{0.004}\right)\right) \text{ Pa}, & \text{if } 0.65 < t < 0.8. \end{cases}$$

We model the left ventricular myocardium as a nonlinear, anisotropic hyperelastic material. To account for the effect of active tension, the first Piola-Kirchhoff stress tensor of the myocardium is modelled as the sum of the active and passive stress,

$$\mathbb{P} = \frac{\partial \Psi}{\partial \mathbb{F}} + \mathbb{P}^a.$$

When the passive stress component is described using the HO model, the active stress component \mathbb{P}^a is given by:

$$\mathbb{P}^a = T(t, I_{4f}) \mathbb{F} \mathbf{e}_f \otimes \mathbf{e}_f,$$

where the scalar tension $T = T(t, I_{4f})$ is a function of time t and I_{4f} . Specifically,

$$T(t, I_{4f}) = T_a(t) \left(1 + 4.9(\sqrt{I_{4f}} - 1)\right),$$

where $T_a(t)$ is the active tension, which is determined empirically. Based on the maximum active tension value of a healthy LV reported in,³ we set its expression according to,³⁰ as follows:

$$T_a(t) = \begin{cases} 0 \text{ Pa}, & \text{if } t < 0.5, \\ 84260 \left(1 - \exp\left(-\frac{(t-0.5)^2}{0.005}\right)\right) \text{ Pa}, & \text{if } 0.5 < t < 0.65, \\ 84260 \left(1 - \exp\left(-\frac{(0.8-t)^2}{0.005}\right)\right) \text{ Pa}, & \text{if } 0.65 < t < 0.8. \end{cases}$$

The detailed physical and numerical parameters are listed in Table 4.

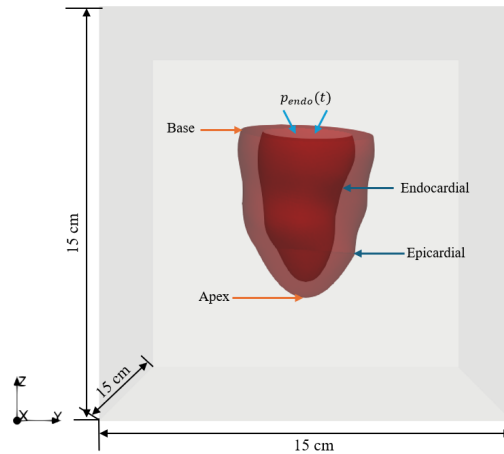


Figure 9: Setup of setting up the LV model in the IB framework: The gray region represents the fixed computational domain Ω , while the red region corresponds to the deformable LV.

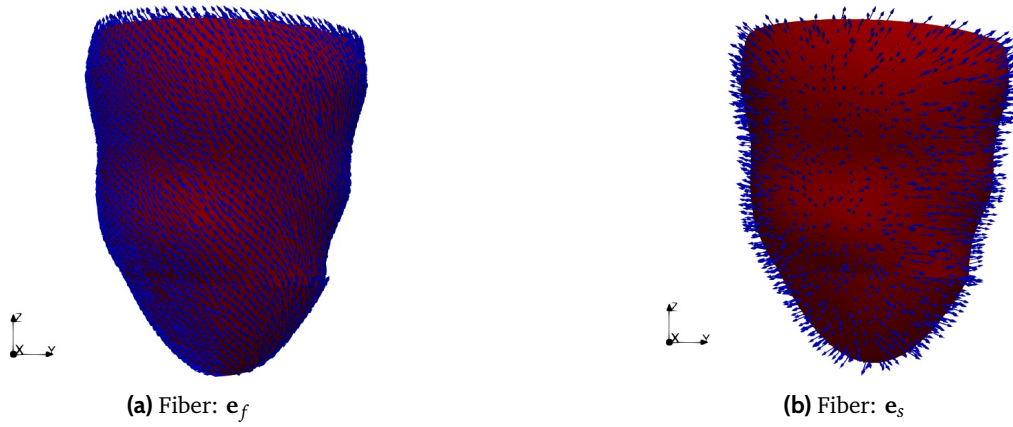


Figure 10: Fiber distribution in the LV model. Blue arrows indicate the direction of fibers, and red represents the LV model.

Symbol	Value	Unit
ρ	1.0	$\frac{\text{g}}{\text{cm}^3}$
T	2.4	s
μ	0.04	$\frac{\text{dyn}\cdot\text{s}}{\text{cm}^2}$
a	2244.87	$\frac{\text{dyn}}{\text{cm}^2}$
a_f	24267	$\frac{\text{dyn}}{\text{cm}^2}$
a_s	5562.38	$\frac{\text{dyn}}{\text{cm}^2}$
a_{fs}	3905.16	$\frac{\text{dyn}}{\text{cm}^2}$
b	1.6215	-
b_f	1.8268	-
b_s	0.7746	-
b_{fs}	1.695	-
κ_s	10^6	-

Table 4: Parameters for the dynamic LV model.

In this model, three consecutive cardiac cycles were simulated, encompassing both the diastolic and systolic phases. Fig. 11 illustrates the deformation of the LV, where Fig. 11b shows the LV in the diastolic phase, and Fig. 11c depicts it in the systolic phase. Fig. 12 presents a cross-sectional view of LV deformation and the corresponding velocity streamlines at 0.12 s, 0.45 s, and 0.72 s. As shown in the Fig. 12, the LV is in the diastolic phase at 0.12 s and 0.45 s, during which blood flows into the ventricular cavity. By 0.45 s, the LV nears its maximal diastolic expansion. The streamline pattern at this moment shows a marked reduction in flow velocity, indicating a decrease in the inflow rate and suggesting that the cavity volume is nearing its peak—reflecting the physiological process of ventricular filling. At 0.72 s, The LV is in the systolic phase, and myocardial contraction ejects blood from the cavity. This is evidenced by the reversal of streamline direction and tissue deformation along the axis of contraction. This behavior corresponds to the typical physiological motion of the LV during the cardiac cycle and highlights the pressure-generating effect of myocardial contraction. Fig. 13a shows the temporal variation of the overall geometric volume of the LV. As myocardial tissue is generally regarded as incompressible under normal physiological conditions, the calculated LV volume remains nearly constant throughout the cardiac cycle—consistent with predictions from a purely solid mechanics model. This

supports the validity of the incompressibility assumption used in the simulation. In contrast, Fig. 13b presents the dynamic variation of the LV cavity volume over time, capturing the volumetric fluctuations associated with the filling and ejection phases. These results emphasize the dynamic characteristics of left ventricular pumping function from a volumetric perspective.

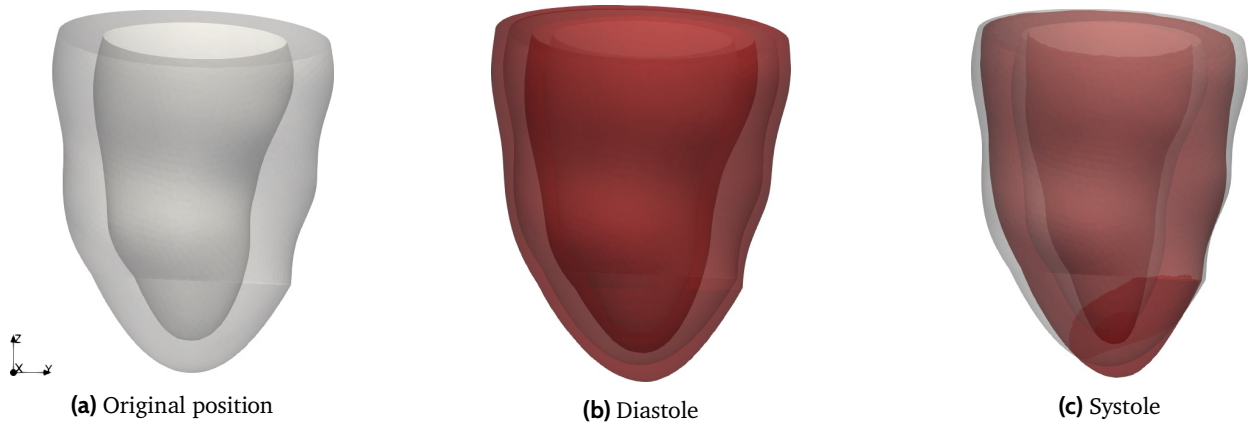


Figure 11: Schematic illustration of left ventricular deformation. The red color indicates the deformed position, while the grey color indicates the original position.

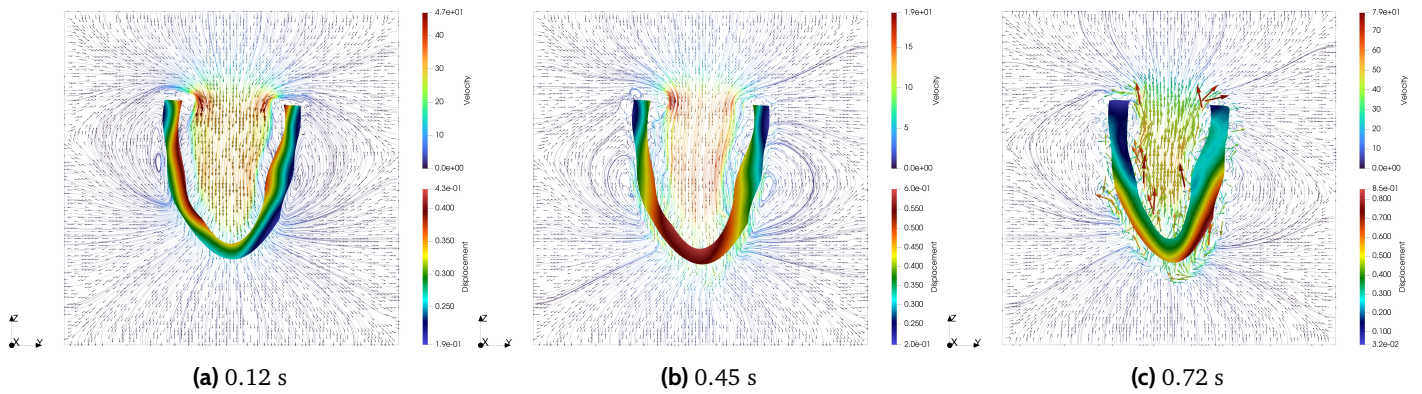


Figure 12: Deformation of a left ventricular slice and fluid velocity streamlines at different times.

5.2 Aortic valve model

The AV is situated between the LV and the aorta, and it plays a critical role in regulating blood ejection from the LV into the aorta during ventricular systole. It also ensures effective closure during diastole to prevent retrograde flow, thereby maintaining the unidirectional circulation of the cardiovascular system. This section further explores the physiological characteristics and functional mechanisms of the AV. The AV consists of three similarly shaped, crescent-like leaflets, each of which is attached at its base to the vessel wall. The basal attachment points of adjacent leaflets converge to form a fibrous structure known as the “annulus.” The posterior aspect of each leaflet interfaces with the aortic wall, which bulges outward to form the aortic sinus.

The mechanical properties of the AV leaflets exhibit pronounced anisotropy, incompressibility, hyperelasticity, and nonlinearity, enabling them to undergo large deformation under physiological loading while maintaining functional stability. Accordingly, to accurately capture these mechanical behaviors, Fiber-reinforced hyperelastic model 2 was employed to characterize the leaflet material response. The AV model used in this section is based on the geometric structure of a porcine heart valve.^{29,36,37} In this model, the leaflet thickness is set to 0.04 cm, and the leaflets are enclosed within a rigid cylindrical tube measuring 14 cm in length, with a wall thickness of 0.15 cm and an inner

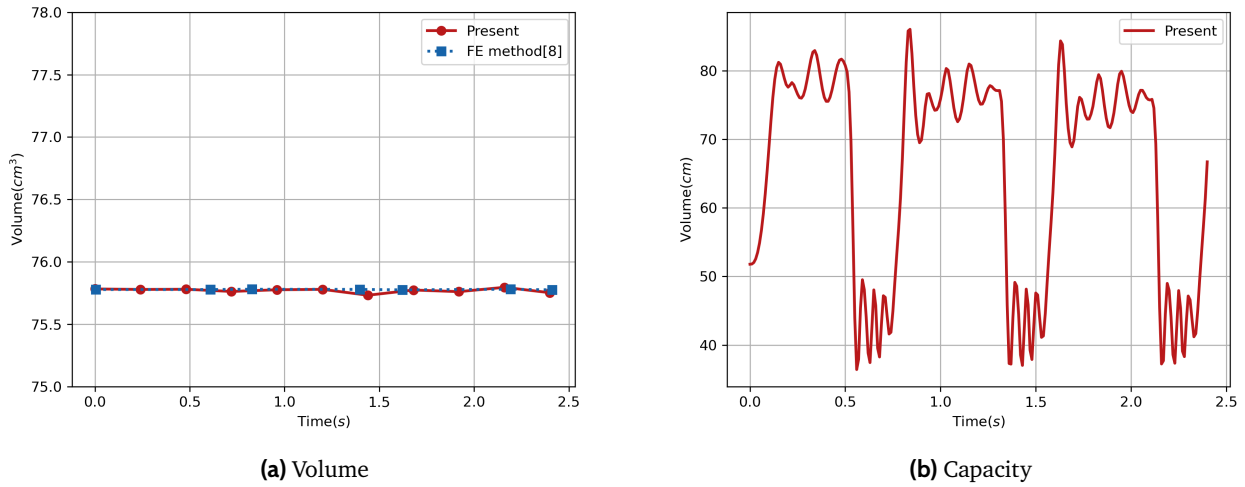


Figure 13: Time-dependent changes in left ventricular volume and ventricular capacity.

	CPU-GPU Heterogeneous		Full GPU (Present)	
	(%)	(s)	(%)	(s)
Poisson equation	71.35	10827.8	57.01	1273
Helmholtz equation	26.99	4095.58	9.85	220
Convective Term	0.34	51.59	0.08	1.873
Interpolation	1.25	189.31	1.16	26
Spreading	1.25	189.31	1.4	46
Solid Solver	1.25	189.31	25.93	579
Total time				2233

Table 5: Execution time distribution of major algorithmic modules in the LV model under different parallelization strategies (CPU–GPU heterogeneous vs. fully GPU-parallel)

radius of 1.3 cm. Fig. 14 presents the complete FSI model, while Fig. 15 illustrates the fiber distribution characteristics of the AV leaflets. In the numerical simulation, the solid domain is discretized into 233,216 tetrahedral elements with 77,530 nodes, and 465,797 basis function nodes are used for the finite element approximation. The fluid domain is discretized using a structured Cartesian grid consisting of $96 \times 96 \times 192$ elements. The relevant physical and numerical parameters are summarized in Table 6.

For this problem, the right end of the outer tube is designated as the inlet, corresponding to the LV, while the left end is the outlet, corresponding to the aorta. The relevant boundary conditions are as follows:

- The physiological pressure of the LV is applied at the inlet of the fluid region to drive blood flow through the AV, with the left ventricular pressure curve shown over one cardiac cycle in Fig. 16a.
- The outlet of the fluid region uses a three-element Windkessel model to apply dynamic pressure loading, as shown in Fig. 16b, driving the AV model. The parameters of the Windkessel model include characteristic resistance $R_c = 0.033 \text{ mmHg} \cdot \text{ml}^{-1} \cdot \text{s}$, peripheral resistance $R_p = 0.79 \text{ mmHg} \cdot \text{ml}^{-1} \cdot \text{s}$, arterial compliance $C = 1.75 \text{ ml} \cdot \text{mmHg}^{-1}$, with an initial pressure of $P_{Wk} = 85 \text{ mmHg}$, and $P_{Ao} = P_{Wk}$, while the outlet pressure is

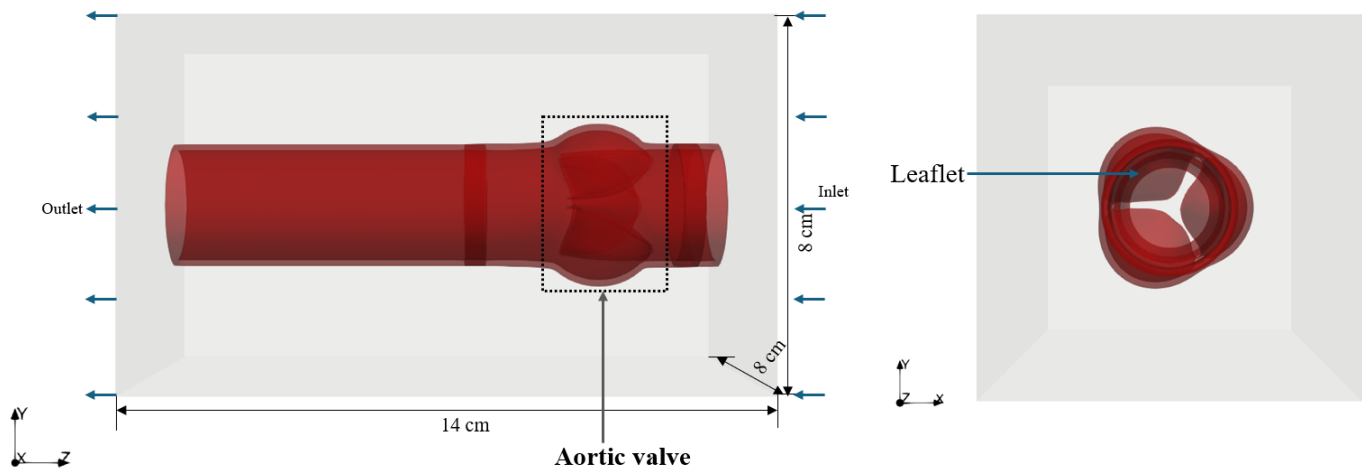


Figure 14: Setup of setting up the AV model in the IB framework: the gray region represents the fixed computational domain Ω , while the red region corresponds to the deformable AV.

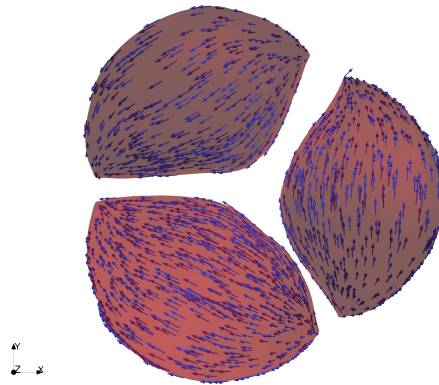


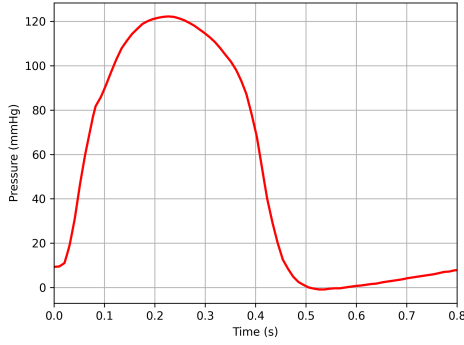
Figure 15: Fiber distribution in the AV model. Blue arrows indicate the direction of fibers, and red represents the AV leaflets.

Symbol	Value	Unit
ρ	1.0	$\frac{g}{ml}$
T	1.635	s
μ	4	cP
C_{10}	1210	Pa
C_{01}	7.99	-
a_f	24230	Pa
b_f	57.62	-
κ_s	10^6	-

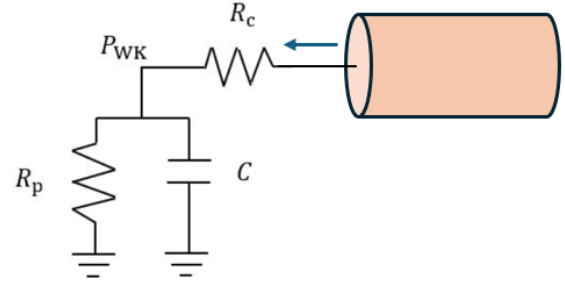
Table 6: Parameters for the AV model.

set to 0. These parameter values are referenced from.^{29,38}

- Zero pressure boundary conditions are applied to the remaining boundaries of the fluid region.



(a) Left ventricular pressure curve at the inlet.



(b) Windkessel model at the outlet

Figure 16: Boundary conditions applied within the AV IB framework.

The numerical simulation of the AV model encompasses two complete cardiac cycles. Fig. 17 presents the dynamic deformation of the valve leaflets, as computed using the algorithm proposed in this study. Figs. 17a and 17b illustrate the leaflet motion during the valve opening phase, whereas Figs. 17c, 17d, and 17e depict the leaflet motion during the valve closure phase. Fig. 18 presents the velocity streamlines and pressure distributions at different time instances. During the valve opening phase, Figs. 18a and 18c illustrate the fluid flow from the LV into the aorta. When the valve is fully open, a pronounced high-velocity jet forms, with a maximum speed of approximately 250 cm/s. Figs. 18b and 18d further show the pressure distribution, where the inlet pressure on the right side is slightly higher than the outlet pressure on the left, thereby driving the transvalvular flow. During the early stage of valve closure, retrograde flow from the aorta (outlet) to the LV (inlet) is observed, as illustrated in Fig. 18e. This reverse flow is driven by a slight pressure elevation at the outlet relative to the inlet, as shown in Fig. 18f. Figs. 18g and 18g depict low-velocity fluid motion within the vessel during this phase, while Figs. 18h and 18j reveal a pronounced transvalvular pressure gradient across the valve leaflets. These observations collectively highlight the dynamic FSI characteristics inherent to the valve closure process.

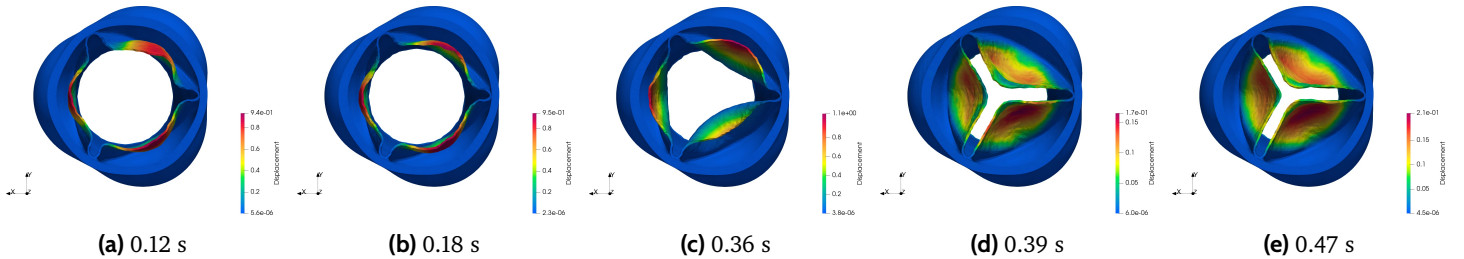


Figure 17: Dynamic deformation of the valve leaflets in the AV model at different time.

Fig. 19 illustrates the time-dependent variation of the flow rate for the AV model over the entire simulation cycle. The results show that the flow rate curve computed using the algorithm proposed in this study exhibits excellent agreement with the reference data reported in.²⁹ Furthermore, the average relative error of the flow rate was quantitatively assessed using the following equation:³⁹

$$\epsilon = \frac{1}{N} \sum_{i=1}^N \left| \frac{Q_i^{\text{GPU}} - Q_i^{\text{ref}}}{\max(Q_j^{\text{ref}})} \right| \times 100\% \quad (24)$$

where $N = 100$ represents the number of sampling points. Q^{GPU} denotes the flow rate calculated by the present GPU algorithm, while Q^{ref} corresponds to the reference data from.²⁹ Compared to the data presented in,²⁹ the average relative error is 3.53%, further validating the accuracy of the proposed algorithm.

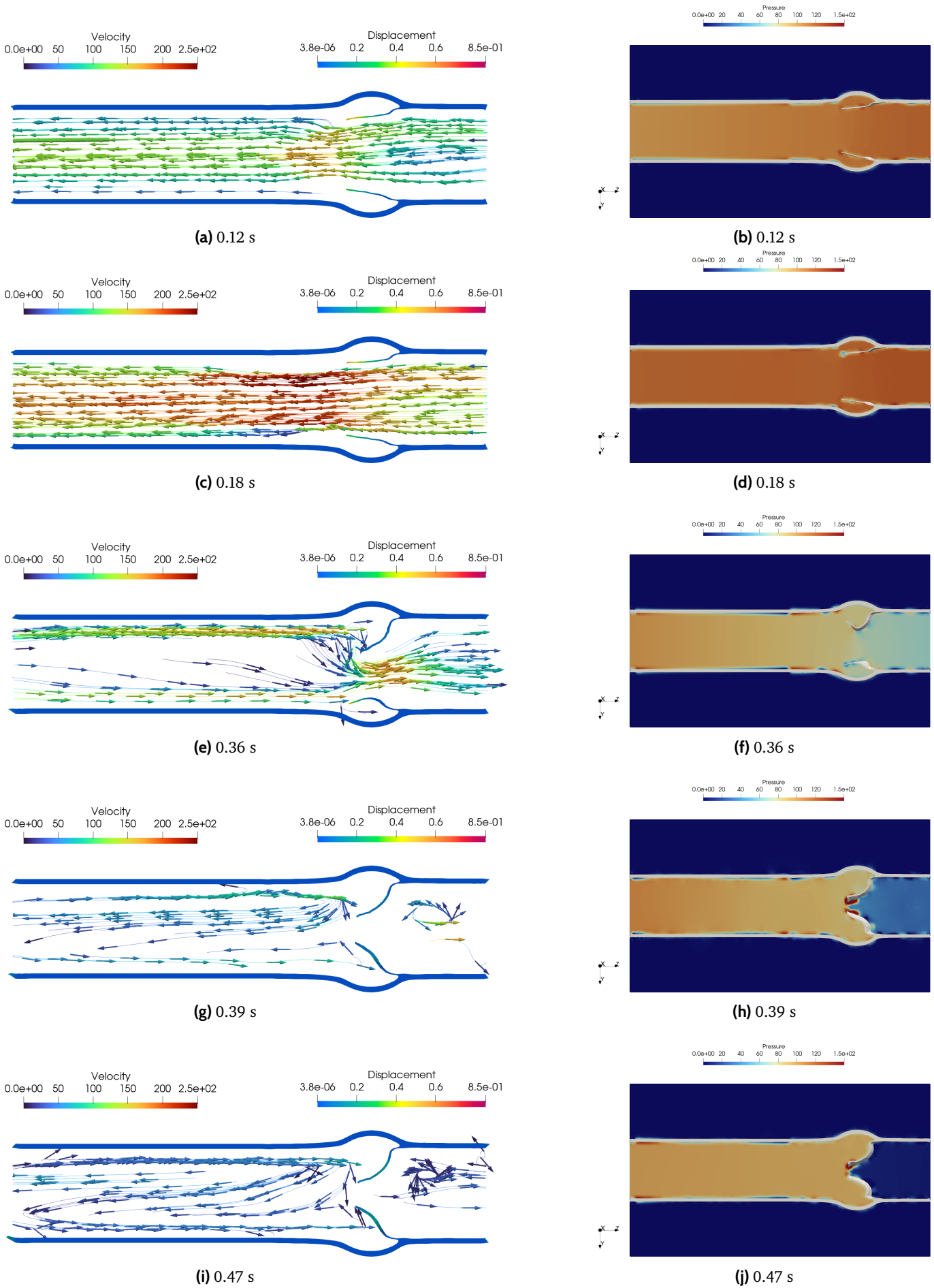


Figure 18: AV model velocity streamlines and pressure distribution. Left: (a), (c), (e) (g), (i) show the velocity streamlines at 0.12 s, 0.18 s, and 0.36 s, 0.39 s, 0.47 s respectively. Right: (b), (d), (f), (h), (j) show the pressure distribution at the same time.

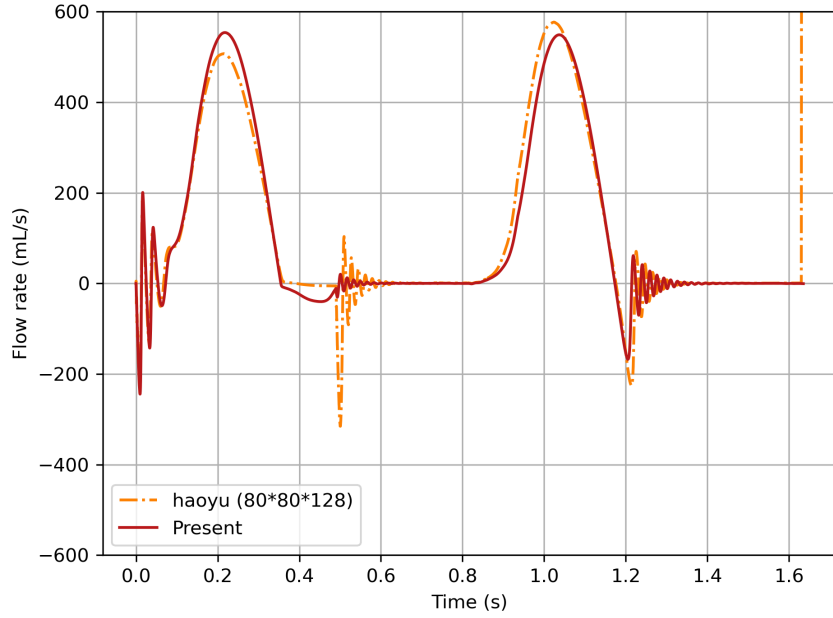


Figure 19: AV model flow rate diagram.

parallel scheme	Device	Number of elements	Time cost(s)	Speed-up ratio
GPU(Present)	RTX4090	233,216	17000	101.02
GPU(Present)	P100	233,216	29000	59.22
GPU(Present)	V100	233,216	27000	63.61
CPU(IBAMR) ¹³	Xeon 5115(×2)	196,029	1717404	1.00

Table 7: Total computational cost of the AV model on different parallel computing platforms.

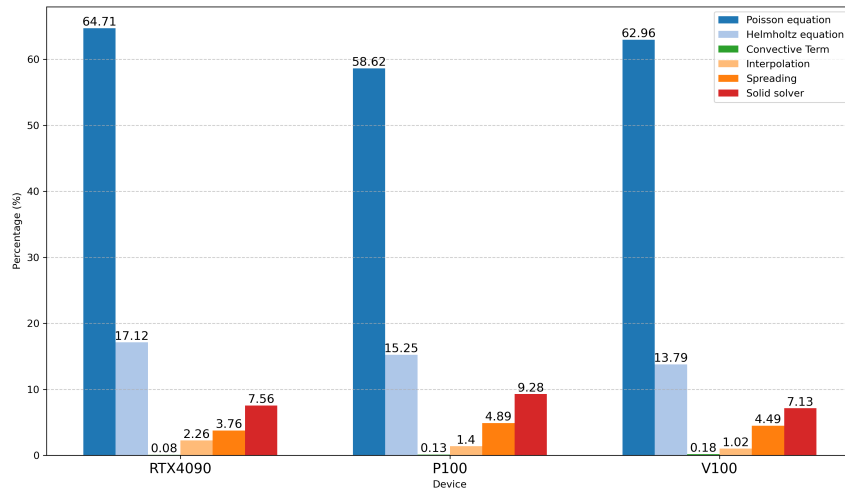


Figure 20: Execution time distribution of the major algorithmic modules in the AV model across various GPU devices.

Table 7 summarizes the computational performance of the proposed algorithm for the AV model across different parallel computing platforms, including the GeForce RTX 4090, Tesla P100, NVIDIA V100, and dual Xeon 5112 CPUs. The

speedup is defined as the ratio of the computation time on each platform to that of the 20-core CPU implementation based on the IBAMR framework, as reported in.¹³ The results show that the RTX 4090 achieves a speedup of approximately 101.02×, while the V100 and P100 achieve about 63.61× and 59.22×, respectively. These findings not only demonstrate the high computational efficiency of the proposed algorithm but also highlight its strong portability and scalability across diverse GPU architectures. In addition, Fig. 20 presents the distribution of execution time among the major algorithmic modules across various GPU platforms. The results show that the Poisson equation solver consistently dominates the computational cost, accounting for more than 58% of the total runtime on all devices. The Helmholtz equation solver is the second most time-consuming component, contributing over 13%, while all other modules consume less than 10% of the total time. These findings further validate the efficiency of the proposed algorithm and underscore its potential for targeted optimization of dominant computational bottlenecks.

5.3 Mitral valve model

The MV is located between the left atrium (LA) and the LV. It opens during diastole to facilitate blood flow into the LV and closes during systole to prevent backflow into the LA. The proper function of the MV is essential for maintaining effective cardiac output and minimizing the hemodynamic load on the heart. This section provides a detailed examination of the MV's physiological function and dynamic behavior. Compared to the AV, the MV has a more complex mechanical structure and tissue characteristics, including two main valve leaflets (anterior and posterior), the mitral annulus, chordae tendineae, and papillary muscles. The structure of the valve leaflets is asymmetric, and the mitral annulus is fixed to the left ventricular wall. The interaction between the valve leaflets and the annulus prevents blood from flowing back into the LA during cardiac contraction. The chordae tendineae connect the valve leaflets to the papillary muscles, primarily controlling the motion of the leaflets; the papillary muscles, fixed to the left ventricular wall, serve as anchor points for the chordae tendineae, further regulating the motion of the valve leaflets. This complex structural interaction is essential for the proper function of the MV.

To accurately characterize the complex mechanical behavior of the MV leaflets—namely their pronounced anisotropy, incompressibility, hyperelasticity, and nonlinearity—we adopt Fiber-reinforced hyperelastic model 1 to model their constitutive response.^{28,40} The mechanical behavior of the chordae tendineae is described using a linear elastic Neo-Hookean model, which reasonably captures their elastic deformation characteristics under physiological conditions.^{28,40} The strain energy function for this model is given by:

$$\Psi = a(\bar{I}_1 - 3) + \frac{\kappa_{\text{stab}}}{2} (\ln(J))^2,$$

and its first Piola-Kirchhoff stress tensor is:

$$\mathbb{P} = 2aJ^{-2/3} (\mathbb{F} - \frac{I_1}{3}\mathbf{F}^{-T}) + \kappa_{\text{stab}} \ln(J) \mathbf{F}^{-T}.$$

This section is based on the previously developed image-based geometric model of the MV.^{28,40,41} In the model, the thickness of the valve leaflets is set to 0.1 cm, and the length of the surrounding rigid circular tube is 16 cm, with a radius of 3.8 cm. The complete FSI model is shown in Fig. 21, and the fiber distribution within the valve leaflets is illustrated in Fig. 22. In the numerical simulations, the solid domain is discretized into 734,645 tetrahedral elements and 188,557 mesh nodes, with 1,245,119 nodes used for basis functions. Meanwhile, the fluid region is discretized into a Cartesian grid of 80 × 80 × 128 elements. The relevant physical and numerical parameters are provided in Table 8.

The boundary conditions for the FSI system of the MV model are set as follows:

- A pressure difference is defined between the inlet and outlet of the tube, with the transvalvular pressure difference based on a typical human physiological pressure curve (as shown in Fig. 23).
- Zero-pressure boundary conditions are applied along the remainder boundaries of the fluid region.^{40,41}

In this MV model, the LV is excluded; therefore, the simulation focuses solely on the rapid filling phase of diastole and the systolic phase. The total computational time is set to represent one complete cardiac cycle, with a duration of

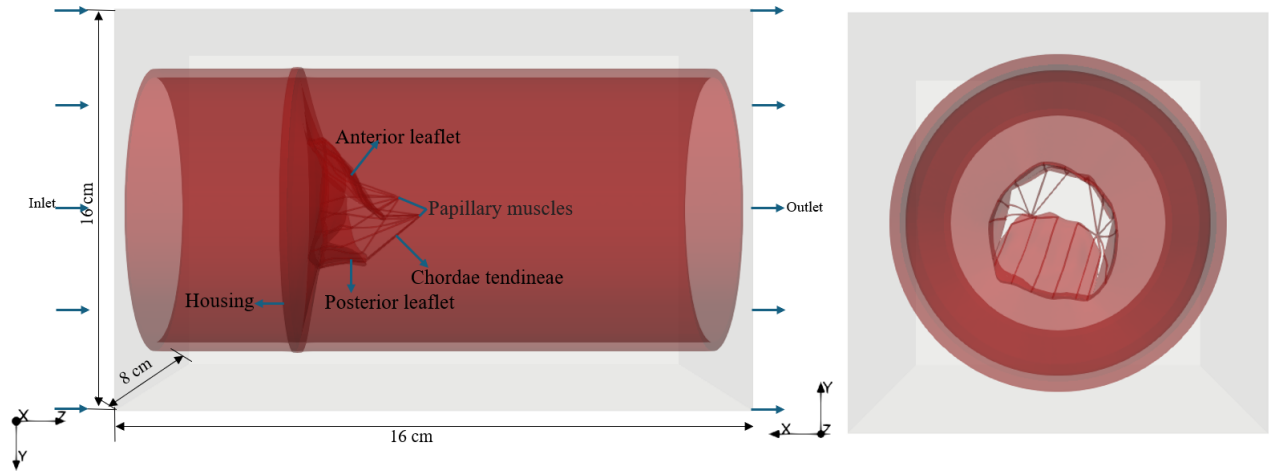


Figure 21: Setup of setting up the MV model in the IB framework: the gray region represents the fixed computational domain Ω , while the red region corresponds to the deformable MV.

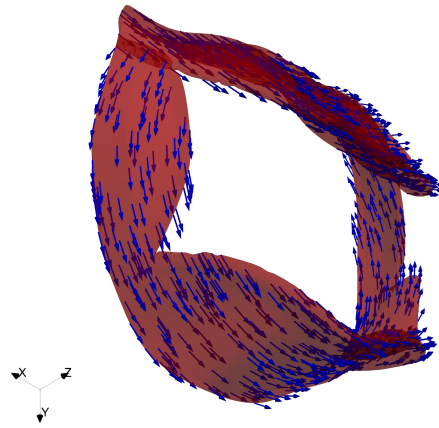


Figure 22: Fiber distribution in the MV model. Blue arrows indicate the direction of fibers, and red represents the MV leaflets.

0.8 s. Using the fully GPU-based algorithm proposed in this study, Fig. 24 illustrates the velocity streamlines, pressure distribution, and the deformation of the MV leaflets and chordae tendineae. As shown in Fig. 24a, when the valve is fully open ($t = 0.1$ s), a strong jet is observed flowing toward the outlet. Meanwhile, Fig. 24d demonstrates that the valve opens under a driving pressure difference of approximately 10 mmHg, accompanied by significant pressure variations near the valve. Fig. 24b indicates that when the valve has just closed ($t = 0.22$ s), regurgitation occurs, which is considered a primary mechanism for the first heart sound.⁴⁰ Fig. 24c presents the velocity distribution at the peak of the transvalvular pressure gradient. Figs. 24e and 24f show that the valve fully closes under a transvalvular pressure difference of approximately 80 mmHg, followed by slight additional deformation as the transmembrane pressure difference further increases to a peak value of 150 mmHg.

Fig. 25 illustrates the temporal evolution of the flow rate over a 0.5 s period for the MV model and presents a comparative analysis between the results obtained using the GPU-based algorithm proposed in this study and the simulation data reported in.^{28,40} The results indicate that the flow rate curve obtained by our method shows excellent agreement with the reference data, demonstrating strong performance in terms of both accuracy and stability. Furthermore, the average relative error of the flow rate was quantitatively evaluated using Eq. (24). Compared with the simulation results in,²⁸ the average relative error is $\epsilon = 3.41\%$, while the comparison with⁴⁰ yields an error of $\epsilon = 4.39\%$. These findings further validate the high accuracy and reliability of the proposed algorithm in predicting flow rate.

Type	Symbol	Value	Unit
-	ρ	1.0	$\frac{g}{cm^3}$
-	T	2	s
-	μ	0.04	$\frac{dyn \cdot s}{cm^2}$
Anterior leaflet	C_1	17400	Pa
Anterior leaflet	a_f	31300	Pa
Anterior leaflet	b_f	55.93	-
-	κ_s	10^6	-
Posterior leaflet	C_1	10200	Pa
Posterior leaflet	a_f	50000	Pa
Posterior leaflet	b_f	63.48	-
-	κ_s	10^6	-
Chordae tendineae(systole)	C	9.0	MPa
Chordae tendineae(diastole)	C	0.54	MPa
-	κ_s	10^6	-

Table 8: Parameters for the MV model.

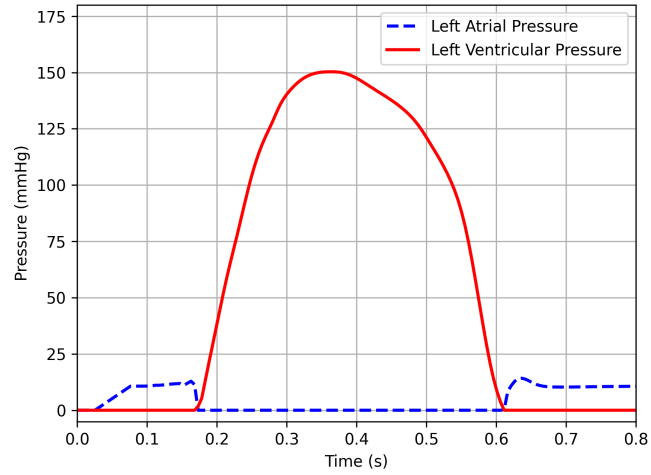


Figure 23: The pressure curves prescribed at the inlet and outlet of the tube in the MV model to define the transvalvular pressure difference.

To evaluate the computational efficiency of the proposed algorithm, a systematic analysis of the simulation runtime for the MV model was conducted on various parallel computing devices (GeForce RTX4090, Tesla P100, NVIDIA V100, and Xeon 5115 $\times 2$ CPUs), with the corresponding data presented in Table 9. Similarly, the speedup ratio is defined as the runtime on each device relative to that of the 20-core CPU implementation using the IBAMR framework described in.¹¹ The results indicate that the proposed IB algorithm demonstrates outstanding computational performance on

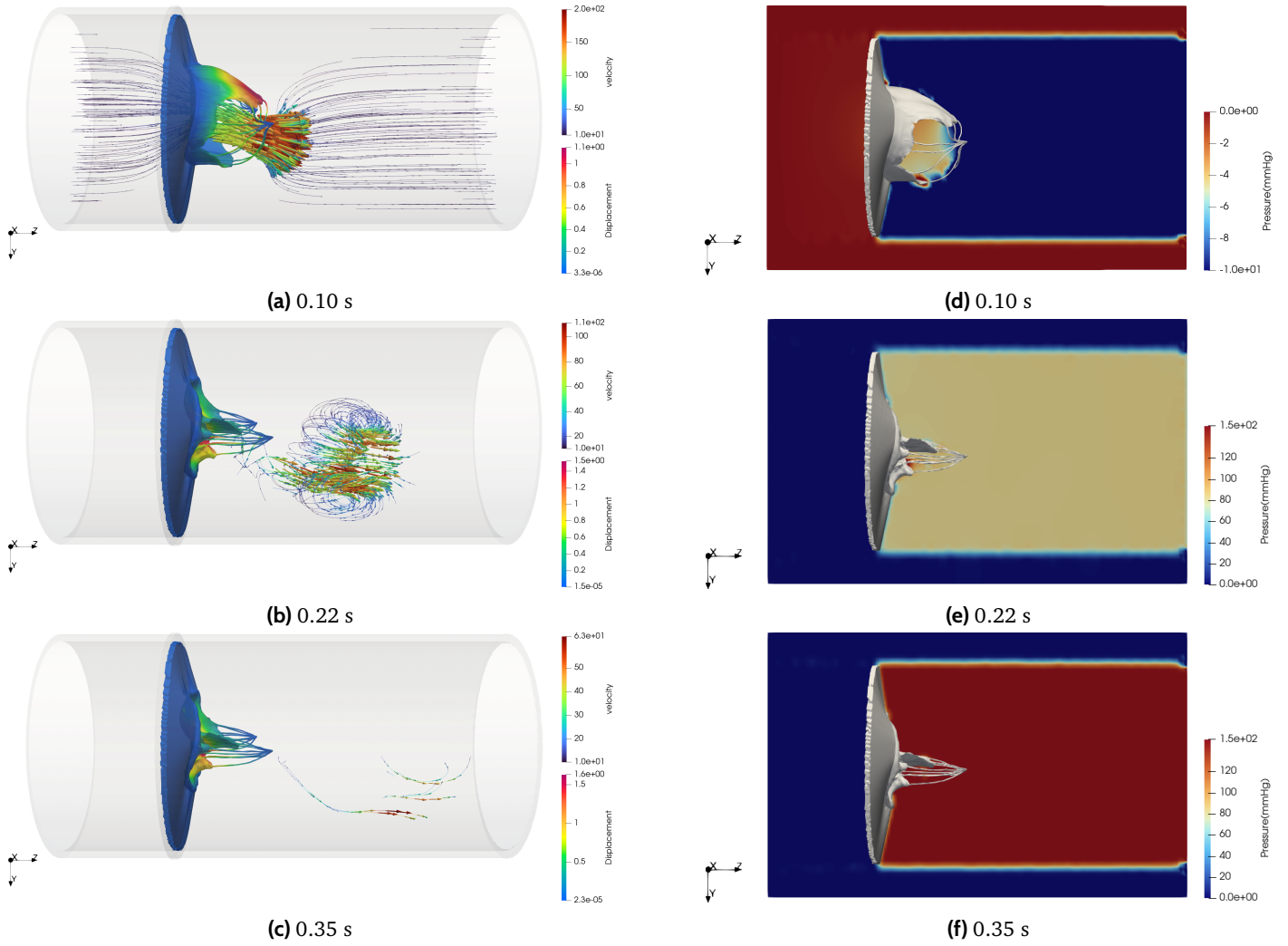


Figure 24: MV model velocity streamlines and pressure distribution. Left: (a), (b), (c) show the velocity streamlines at 0.1 s, 0.22 s, and 0.35 s, respectively. Right: (d), (e), (f) show the pressure distribution at the same time.

parallel scheme	Device	Number of elements	Time cost(s)	Speed-up ratio
GPU(Present)	RTX4090	734,645	2908	57.28
GPU(Present)	P100	734,645	5751	28.96
GPU(Present)	V100	734,645	4726	35.24
CPU(IBAMR) ¹³	Xeon 5115(×2)	260,053	166559	1.00

Table 9: Total computational cost of the MV model on different parallel computing platforms.

GPU platforms: the simulation on the RTX4090 achieves a speedup of 57.4× compared to the 20-core CPU, while the P100 and V100 achieve speedups of 28.96× and 35.24×, respectively, clearly highlighting the efficiency of the proposed method on various GPU platforms. Furthermore, a detailed comparison of the runtime distribution across major algorithm modules was performed on different GPU devices, as illustrated in Fig. 26. The analysis indicates that solving the Poisson equation remains the most time-consuming component of the computation, consistently accounting for over 47% of the total runtime across all GPU devices. The solid structure solver also contributes more than 15% of the total computational cost. Compared with the AV model, this increased cost is likely due to the denser solid

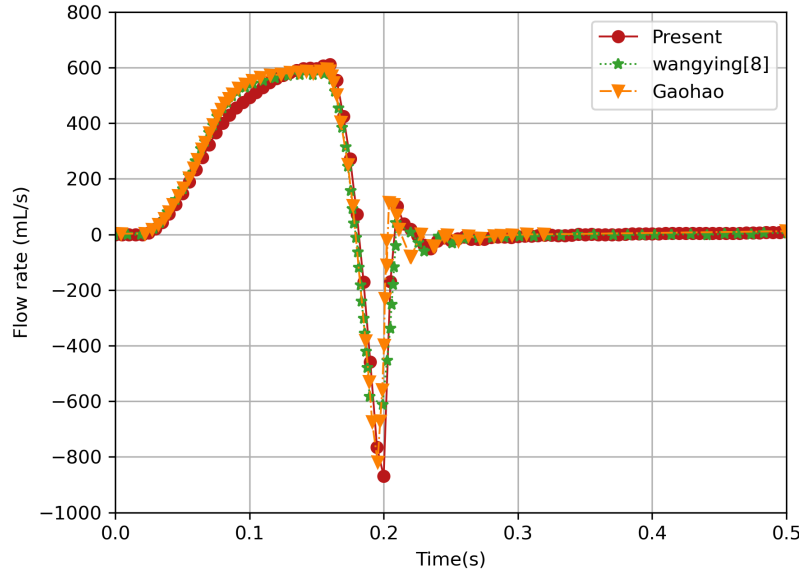


Figure 25: MV model flow rate diagram.

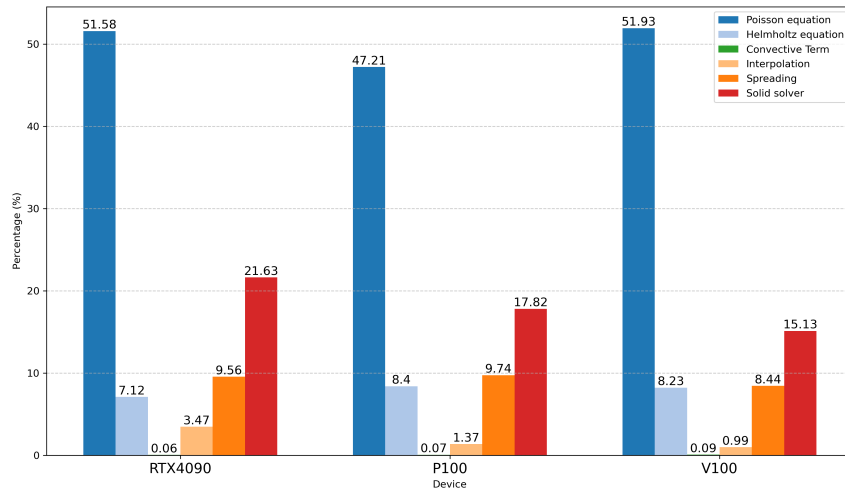


Figure 26: Execution time distribution of the major algorithmic modules in the MV model across various GPU devices.

mesh, more complex geometry, and the inherent nonlinearity and computational demands of the solid mechanics model. In contrast, with the support of GPU acceleration, the execution times of the remaining functional modules are significantly reduced, each accounting for less than 10% of the total runtime. These findings further demonstrate the effectiveness of the proposed algorithm in enhancing overall computational performance.

6 Conclusions

This study presents a fully GPU-accelerated IB framework that enables high-fidelity FSI simulations of complex cardiac mechanics on consumer-grade hardware. The framework introduces three key methodological advancements: (1) an IB-based FSI formulation for modeling soft cardiac tissue as a fiber-reinforced hyperelastic material on GPU, distinguishing it from membrane-based or purely fiber-based models; (2) a memory hierarchy-aware GPU implementation strategy, optimizing finite element basis storage in constant memory and mapping convective terms via texture memory; and

(3) a reformulated Navier-Stokes solver tailored for the IB method that combines geometric multigrid with optimized Gauss-Seidel iterations, fully eliminating sparse matrix operations for efficient GPU execution.

Comprehensive validation across cardiac models demonstrates unprecedented computational efficiency without compromising biomechanical fidelity. Benchmark results show consistent 50–100× speedups over 20-core CPU implementations, reducing mitral valve simulations from days to just 48 minutes on a single RTX 4090 GPU. The framework maintains near-perfect volume conservation (maximum deviation: 0.0088%) in anisotropic Cook’s membrane tests and achieves clinically relevant accuracy about the aortic valve, with flow rate deviations under 4.4% compared to prior numerical calculations. The framework systematically captures intricate physiological phenomena—including mitral regurgitation jets, aortic leaflet coaptation dynamics, and myocardial fiber-mediated ventricular torsion.

By significantly reducing computational time, our approach lowers barriers to patient-specific cardiac modeling. Full-cycle valve simulations, which previously took days, can now be completed within hours—establishing a foundation for real-time surgical planning and medical device optimization. Future extensions aim to integrate medical imaging pipelines and extend the framework to whole-heart simulations.

Author contributions

Pengfei Ma: Methodology (lead); Software(lead); Writing - original draft (lead). **Li Cai:** Supervision (lead); Writing - review & editing (equal). **Xuan Wang:** Visualization (lead); Writing - original draft (supporting); Writing - review & editing (equal). **Hao Gao:** Writing - review & editing (equal).

Declaration of competing interest

The authors declare that they have no known competing financial interests or personal relationships that could have appeared to influence the work reported in this paper.

Data availability

Data will be made available on request.

Acknowledgements

Xuan Wang, Li Cai and Pengfei Ma were supported by the National Natural Science Foundation of China (Grant No. 12271440). Hao Gao was supported by the British Heart Foundation (PG/22/10930) and the Engineering and Physical Sciences Research Council (EPSRC) of the United Kingdom (EP/S030875/1). Pengfei Ma was supervised by the late Professor Xiaoyu Luo during this research.

References

- ¹ Boyce E Griffith. Immersed boundary model of aortic heart valve dynamics with physiological driving and loading conditions. *International journal for numerical methods in biomedical engineering*, 28(3):317–345, 2012.
- ² Hao Gao, Nan Qi, Xingshuang Ma, Boyce E Griffith, Colin Berry, and Xiaoyu Luo. Fluid-structure interaction model of human mitral valve within left ventricle. In *Functional Imaging and Modeling of the Heart: 8th International Conference, FIMH 2015, Maastricht, The Netherlands, June 25-27, 2015. Proceedings 8*, pages 330–337. Springer, 2015.
- ³ Hao Gao, David Carrick, Colin Berry, Boyce E Griffith, and Xiaoyu Luo. Dynamic finite-strain modelling of the human left ventricle in health and disease using an immersed boundary-finite element method. *IMA journal of applied mathematics*, 79(5):978–1010, 2014.

- ⁴ Liuyang Feng, Hao Gao, and Xiaoyu Luo. Whole-heart modelling with valves in a fluid–structure interaction framework. *Computer Methods in Applied Mechanics and Engineering*, 420:116724, 2024.
- ⁵ Li Cai, Tong Zhao, Yongheng Wang, Xiaoyu Luo, and Hao Gao. Fluid–structure interaction simulation of pathological mitral valve dynamics in a coupled mitral valve-left ventricle model. *Intelligent Medicine*, 3(2):104–114, 2023.
- ⁶ Liuyang Feng, Hao Gao, Nan Qi, Mark Danton, Nicholas A Hill, and Xiaoyu Luo. Fluid–structure interaction in a fully coupled three-dimensional mitral–atrium–pulmonary model. *Biomechanics and modeling in mechanobiology*, 20:1267–1295, 2021.
- ⁷ Marshall Davey, Charles Puelz, Simone Rossi, Margaret Anne Smith, David R Wells, Gregory M Sturgeon, W Paul Segars, John P Vavalle, Charles S Peskin, and Boyce E Griffith. Simulating cardiac fluid dynamics in the human heart. *PNAS nexus*, 3(10):pgae392, 2024.
- ⁸ Charles S Peskin. Flow patterns around heart valves: a numerical method. *Journal of computational physics*, 10(2):252–271, 1972.
- ⁹ Charles S Peskin. Numerical analysis of blood flow in the heart. *Journal of computational physics*, 25(3):220–252, 1977.
- ¹⁰ Daniele Boffi, Lucia Gastaldi, Luca Heltai, and Charles S Peskin. On the hyper-elastic formulation of the immersed boundary method. *Computer Methods in Applied Mechanics and Engineering*, 197(25-28):2210–2231, 2008.
- ¹¹ Boyce E Griffith and Xiaoyu Luo. Hybrid finite difference/finite element immersed boundary method. *International journal for numerical methods in biomedical engineering*, 33(12):e2888, 2017.
- ¹² Ben Vadala-Roth, Shashank Acharya, Neelesh A Patankar, Simone Rossi, and Boyce E Griffith. Stabilization approaches for the hyperelastic immersed boundary method for problems of large-deformation incompressible elasticity. *Computer methods in applied mechanics and engineering*, 365:112978, 2020.
- ¹³ Boyce E Griffith. Ibamr: an adaptive and distributed-memory parallel implementation of the immersed boundary method. 2014. URL <https://github.com/IBAMR/IBAMR>, 2017.
- ¹⁴ Boyce E Griffith, Richard D Hornung, David M McQueen, and Charles S Peskin. Parallel and adaptive simulation of cardiac fluid dynamics. *Advanced computational infrastructures for parallel and distributed adaptive applications*, 105, 2010.
- ¹⁵ NVIDIA. Cuda c++ programming guide. *NVIDIA*, July, 2020.
- ¹⁶ Simon K Layton, Anush Krishnan, and Lorena A Barba. cuibm—a gpu-accelerated immersed boundary method. *arXiv preprint arXiv:1109.3524*, 2011.
- ¹⁷ Francesco Viola, Vamsi Spandan, Valentina Meschini, Joshua Romero, Massimiliano Fatica, Marco D de Tullio, and Roberto Verzicco. Fsei-gpu: Gpu accelerated simulations of the fluid–structure–electrophysiology interaction in the left heart. *Computer physics communications*, 273:108248, 2022.
- ¹⁸ Manuel Guerrero-Hurtado, Juan Manuel Catalan, Manuel Moriche, A Gonzalo, and O Flores. A python-based flow solver for numerical simulations using an immersed boundary method on single gpus. *Computers & Fluids*, 288:106511, 2025.
- ¹⁹ Fei Jiang, Kazuki Matsumura, Junji Ohgi, and Xian Chen. A gpu-accelerated fluid–structure-interaction solver developed by coupling finite element and lattice boltzmann methods. *Computer Physics Communications*, 259:107661, 2021.

- ²⁰ Jae H Lee, Alex D Rygg, Ebrahim M Kolahdouz, Simone Rossi, Stephen M Retta, Nandini Duraiswamy, Lawrence N Scotten, Brent A Craven, and Boyce E Griffith. Fluid–structure interaction models of bioprosthetic heart valve dynamics in an experimental pulse duplicator. *Annals of biomedical engineering*, 48:1475–1490, 2020.
- ²¹ David R Wells, Ben Vadala-Roth, Jae H Lee, and Boyce E Griffith. A nodal immersed finite element-finite difference method. *Journal of computational physics*, 477:111890, 2023.
- ²² Jos Stam. Stable fluids. In *Seminal Graphics Papers: Pushing the Boundaries, Volume 2*, pages 779–786. 2023.
- ²³ Charles S Peskin. The immersed boundary method. *Acta numerica*, 11:479–517, 2002.
- ²⁴ Robert S Strichartz. *A guide to distribution theory and Fourier transforms*. World Scientific Publishing Company, 2003.
- ²⁵ Pengfei Ma, Li Cai, Xuan Wang, Yongheng Wang, Xiaoyu Luo, and Hao Gao. An unconditionally stable scheme for the immersed boundary method with application in cardiac mechanics. *Physics of Fluids*, 36(8), 2024.
- ²⁶ Lianxia Li, Cole Gruninger, Jae H Lee, and Boyce E Griffith. Local divergence-free immersed finite element-difference method using composite b-splines. *arXiv preprint arXiv:2412.15408*, 2024.
- ²⁷ Javier Bonet and Richard D Wood. *Nonlinear continuum mechanics for finite element analysis*. Cambridge university press, 1997.
- ²⁸ Li Cai, Ying Wang, Hao Gao, Xingshuang Ma, Guangyu Zhu, Ruihang Zhang, Xiaoqin Shen, and Xiaoyu Luo. Some effects of different constitutive laws on fsi simulation for the mitral valve. *Scientific Reports*, 9(1):12753, 2019.
- ²⁹ Li Cai, Ruihang Zhang, Yiqiang Li, Guangyu Zhu, Xingshuang Ma, Yongheng Wang, Xiaoyu Luo, and Hao Gao. The comparison of different constitutive laws and fiber architectures for the aortic valve on fluid–structure interaction simulation. *Frontiers in Physiology*, 12:682893, 2021.
- ³⁰ Namshad Thekkethil, Simone Rossi, Hao Gao, Scott I Heath Richardson, Boyce E Griffith, and Xiaoyu Luo. A stabilized linear finite element method for anisotropic poroelastodynamics with application to cardiac perfusion. *Computer methods in applied mechanics and engineering*, 405:115877, 2023.
- ³¹ Elijah P Newren, Aaron L Fogelson, Robert D Guy, and Robert M Kirby. Unconditionally stable discretizations of the immersed boundary equations. *Journal of Computational Physics*, 222(2):702–719, 2007.
- ³² Duc-Vinh Le, J White, Jaime Peraire, Kian Meng Lim, and BC Khoo. An implicit immersed boundary method for three-dimensional fluid–membrane interactions. *Journal of computational physics*, 228(22):8427–8445, 2009.
- ³³ Hao Gao, Andrej Aderhold, Kenneth Mangion, Xiaoyu Luo, Dirk Husmeier, and Colin Berry. Changes and classification in myocardial contractile function in the left ventricle following acute myocardial infarction. *Journal of The Royal Society Interface*, 14(132):20170203, 2017.
- ³⁴ Hao Gao, Huiming Wang, Colin Berry, Xiaoyu Luo, and Boyce E Griffith. Quasi-static image-based immersed boundary-finite element model of left ventricle under diastolic loading. *International journal for numerical methods in biomedical engineering*, 30(11):1199–1222, 2014.
- ³⁵ Li Cai, Hao Gao, Xiaoyu Luo, and Yufeng Nie. Multi-scale modelling of the human left ventricle. *Scientia Sinica Physica, Mechanica and Astronomica*, 45(2), 2015.
- ³⁶ Guangyu Zhu, Masakazu Nakao, Qi Yuan, and Joon Hock Yeo. In-vitro assessment of expanded-polytetrafluoroethylene stentless tri-leaflet valve prosthesis for aortic valve replacement. In *International Conference on Biomedical Electronics and Devices*, volume 2, pages 186–189. SCITEPRESS, 2017.
- ³⁷ Vittoria Flamini, Abe DeAnda, and Boyce E Griffith. Immersed boundary-finite element model of fluid–structure interaction in the aortic root. *Theoretical and computational fluid dynamics*, 30:139–164, 2016.

- ³⁸ Nikos Stergiopoulos, Berend E Westerhof, and Nico Westerhof. Total arterial inertance as the fourth element of the windkessel model. *American Journal of Physiology-Heart and Circulatory Physiology*, 276(1):H81–H88, 1999.
- ³⁹ Yao Lu, Peishuo Wu, Moubin Liu, and Chi Zhu. A gpu-accelerated 3d isph-tlsph framework for patient-specific simulations of cardiovascular fluid–structure interactions. *Computer Methods in Applied Mechanics and Engineering*, 428:117110, 2024.
- ⁴⁰ Hao Gao, Xingshuang Ma, Nan Qi, Colin Berry, Boyce E Griffith, and Xiaoyu Luo. A finite strain nonlinear human mitral valve model with fluid-structure interaction. *International journal for numerical methods in biomedical engineering*, 30(12):1597–1613, 2014.
- ⁴¹ Xingshuang Ma, Hao Gao, Boyce E Griffith, Colin Berry, and Xiaoyu Luo. Image-based fluid–structure interaction model of the human mitral valve. *Computers & Fluids*, 71:417–425, 2013.